A multicomponent matched filter cluster confirmation tool for eROSITA: initial application to the RASS and DES-SV data sets

M. Klein, J.J. Mohr, S. Desai, H. Israel, S. Allam, A. Benoit-Lévy, D. Brooks, E. Buckley-Geer, A. Carnero Rosell, M. Carrasco Kind, et al.

Monthly Notices of the ROYAL ASTRONOMICAL SOCIETY

MNRAS **474,** 3324–3343 (2018) doi:10.1093/mnras/stx2929
Advance Access publication 2017 November 14

A multicomponent matched filter cluster confirmation tool for eROSITA: initial application to the RASS and DES-SV data sets

M. Klein,[1,2]★ J. J. Mohr,[1,2,3] S. Desai,[4] H. Israel,[1] S. Allam,[5] A. Benoit-Lévy,[6,7,8] D. Brooks,[7] E. Buckley-Geer,[5] A. Carnero Rosell,[9,10] M. Carrasco Kind,[11,12] C. E. Cunha,[13] L. N. da Costa,[9,10] J. P. Dietrich,[1,3] T. F. Eifler,[14] A. E. Evrard,[15,16] J. Frieman,[5,17] D. Gruen,[13,18] R. A. Gruendl,[11,12] G. Gutierrez,[5] K. Honscheid,[19,20] D. J. James,[21,22] K. Kuehn,[23] M. Lima,[9,24] M. A. G. Maia,[9,10] M. March,[25] P. Melchior,[26] F. Menanteau,[11,12] R. Miquel,[27,28] A. A. Plazas,[14] K. Reil,[18] A. K. Romer,[29] E. Sanchez,[30] B. Santiago,[9,31] V. Scarpine,[5] M. Schubnell,[16] I. Sevilla-Noarbe,[30] M. Smith,[32] M. Soares-Santos,[5] F. Sobreira,[9,33] E. Suchyta,[34] M. E. C. Swanson,[12] G. Tarle[16] and the DES Collaboration[16]

Affiliations are listed at the end of the paper

Accepted 2017 November 9. Received 2017 November 9; in original form 2017 June 17

ABSTRACT

We describe a multicomponent matched filter (MCMF) cluster confirmation tool designed for the study of large X-ray source catalogues produced by the upcoming X-ray all-sky survey mission eROSITA. We apply the method to confirm a sample of 88 clusters with redshifts $0.05 < z < 0.8$ in the recently published 2RXS catalogue from the *ROSAT* All-Sky Survey (RASS) over the 208 deg^2 region overlapped by the Dark Energy Survey (DES) Science Verification (DES-SV) data set. In our pilot study, we examine all X-ray sources, regardless of their extent. Our method employs a multicolour red sequence (RS) algorithm that incorporates the X-ray count rate and peak position in determining the region of interest for follow-up and extracts the positionally and colour-weighted optical richness $\lambda_{\rm MCMF}$ as a function of redshift for each source. Peaks in the $\lambda_{\rm MCMF}$–redshift distribution are identified and used to extract photometric redshifts, richness and uncertainties. The significances of all optical counterparts are characterized using the distribution of richnesses defined along random lines of sight. These significances are used to extract cluster catalogues and to estimate the contamination by random superpositions of unassociated optical systems. The delivered photometric redshift accuracy is $\delta z/(1+z) = 0.010$. We find a well-defined X-ray luminosity–$\lambda_{\rm MCMF}$ relation with an intrinsic scatter of $\delta \ln(\lambda_{\rm MCMF}|L_{\rm x}) = 0.21$. Matching our catalogue with the DES-SV redMaPPer catalogue yields good agreement in redshift and richness estimates; comparing our catalogue with the South Pole Telescope (SPT) selected clusters shows no inconsistencies. SPT clusters in our data set are consistent with the high-mass extension of the RASS-based $\lambda_{\rm MCMF}$–mass relation.

Key words: galaxies: clusters: general – galaxies: clusters: intracluster medium – galaxies: distances and redshifts – X-rays: galaxies: clusters.

1 INTRODUCTION

The abundance of galaxy clusters over a range of mass and redshift is a powerful probe of the amplitude of mass fluctuations in the Universe (White, Efstathiou & Frenk 1993) that is well suited for studies of the cosmic acceleration (Wang & Steinhardt 1998;

★ E-mail: Matthias.Klein@physik.uni-muenchen.de

Haiman, Mohr & Holder 2001; Vikhlinin et al. 2009; Mantz et al. 2010a; de Haan et al. 2016) and consistency tests of the ΛCDM and wCDM paradigms (Rapetti et al. 2010; Bocquet et al. 2015). In addition, galaxy clusters provide the tightest constraints on the dark matter self-interaction cross-section to date (Sartoris et al. 2014; Robertson, Massey & Eke 2017) and offer many other insights into plasma physics and galaxy evolution. To use clusters for these various purposes, the clusters have to be first identified and their redshifts have to be measured.

One common challenge for most recent and upcoming cluster surveys is the large number of cluster candidates. One of these surveys is the eROSITA (Predehl et al. 2010) all sky X-ray survey, which will enable the selection of clusters using the X-ray emission from the hot plasma that fills the gravitational potential wells. The expected number of cluster candidates is $\sim 10^5$ (Merloni et al. 2012). Only a fraction of these candidates will have enough detected X-ray photons to enable a reliable redshift from X-rays alone. The majority, especially at high redshift and low mass, will require optical photometric redshift estimation. The Dark Energy Survey (DES; Dark Energy Survey Collaboration et al. 2016) data set will provide this information for the majority of the overlapping eROSITA cluster candidates. Given the size of the sample and the need to precisely understand the selection for a cosmological analysis of the clusters, an automated and objective follow-up method is therefore needed.

In this analysis, we present a matched filter method for finding the optical counterparts of an X-ray-detected cluster sample. The method leverages the simple time evolution and clustering of the passive galaxy population in clusters. These so-called red sequence (RS) galaxies have been used previously to create large samples of clusters and groups for studies of cosmology (Gladders & Yee 2000; Gladders et al. 2007; Rozo et al. 2010; Rykoff et al. 2014). Our method adopts the prior positional and flux information from the candidate selection in the X-ray when searching for a candidate. It allows for multiple optical counterparts for each candidate cluster, ranking them by the strength of their signal, given the prior X-ray information. Finally, we quantify for each counterpart the probability that it is a random superposition of a physically unassociated structure along the line of sight towards an X-ray cluster candidate. This information can be incorporated in cosmological analyses of the sample.

The *ROSAT* All-Sky Survey (RASS; Truemper 1982) is currently the best available all-sky X-ray survey. We therefore adopt faint source catalogues extracted from RASS to perform a systematic test of our algorithm. To do so we focus on a contiguous area of the DES Science Verification (DES-SV) data set that overlaps the eastern side of the South Pole Telescope (SPT) survey area. This area was observed during the first commissioning and verification campaign with DECam (Flaugher et al. 2015). While the DES-SV data are somewhat shallower than the expected DES final depth, the data set provides the best representation of the final data set currently available. The DES-SV footprint is shown in Fig. 1.

In this paper, we describe the data (Section 2) and method (Section 3) and its current performance (Section 4) in verifying clusters and measuring their redshifts as part of an automated X-ray follow-up. We examine the impact of contaminating stars (Section 4.1) and characterize the cluster sample we extract from the RASS+DES-SV analysis (Section 4.2). In Section 5, we present our conclusions and comment on the expected number of clusters when applying our method to the full DES area. Throughout this paper, we adopt a flat ΛCDM cosmology with $\Omega_M = 0.3$ and $H_0 = 70\,\mathrm{km\,s^{-1}\,Mpc^{-1}}$.

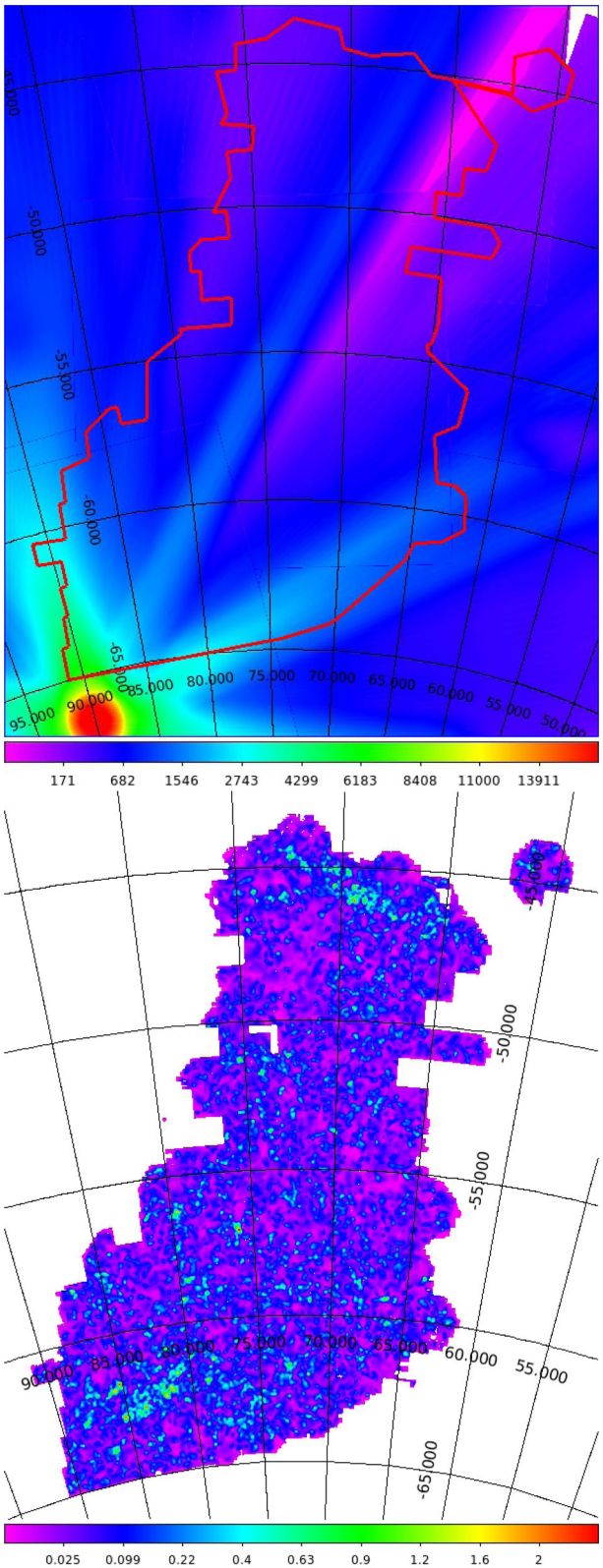

Figure 1. Illustration of the DES-SV footprint. Top panel: DES-SV footprint overlaid on RASS exposure time map. The average exposure time increases from north-west to south-east. The southern ecliptic pole is visible as high exposure time region of the SV area. Colour coded is the exposure time in seconds. Bottom panel: Smoothed weighted density map of galaxies with colours consistent with the RS at $z = 0.12$. Galaxies are weighted by their colour distance to the RS according to equation (8).

2 DATA

The data reduction and catalogue creation follow closely that described in Hennig et al. (2017a). We therefore provide only a brief summary of the methods and data quality here.

2.1 Observations and data reduction

The DES-SV data were acquired between 2012 November 1 and 2013 February. The data reduction is performed using our Cosmology Data Management system (CosmoDM), which is an improved version of the system used to process the Blanco Cosmology Survey Data (Desai et al. 2012) and is a prototype for the development of a data management system being prepared within the Euclid collaboration (Laureijs et al. 2011). The data are first processed on a night-by-night basis, where cross-talk, bias and flat corrections are applied. Each CCD is considered separately; by correcting for varying pixel scale and the resulting persistent variation in sensitivity within each band, we reduce the positional variation of the zero-point within each detector. We measure the persistent variation in sensitivity using star flats extracted using a subset of photometric exposures over the DES-SV period (Regnault et al. 2009; Schlafly et al. 2012; Hennig et al. 2017a).

A first astrometric calibration is performed on the individual exposures using SCAMP (Bertin 2006) with 2-Micron All-Sky Survey (2MASS; Skrutskie et al. 2006) as the absolute reference catalogue. We employ a high-quality distortion map that is derived from a large set of overlapping exposures. The residual scatter between our data and 2MASS is about 200 mas and is dominated by the positional accuracy of the reference catalogue. Within our system, a second astrometric calibration can be performed prior to the co-addition process using all overlapping exposures of a given tile. This second pass internal calibration results in an internal scatter of about 20 mas (less than a tenth of the pixel scale) around the best astrometric solution. For the photometry presented here, this second correction was not applied, because our tests indicate no significant differences in the galaxy photometry with and without the correction.

For the SPT-East field of the DES-SV data set, we create co-adds with tilings of size 62 arcmin × 62 arcmin on a grid with centre offsets of 1°. Neighbouring tiles overlap each other by about 2 arcmin. The relative calibration of all single epoch images contributing to a tile is carried out for each tile independently, and the repeatability of the resulting calibrated single epoch stellar photometry is excellent (see Hennig et al. 2017a).

The co-adds are created from point spread function (PSF)-homogenized single-epoch images where the target PSF is described by a Moffat function (Moffat 1972) with full width at half-maximum (FWHM) tuned to be the median of all contributing images within a single band. The co-adds we employ for this analysis are median-combined to remove all artefacts. Following our previous work, the absolute photometric calibration is obtained using the stellar locus, where the absolute zero-point comes from the 2MASS J band (Desai et al. 2012; Song et al. 2012; Liu et al. 2015). We use an enhanced version of SExtractor (Bertin & Arnouts 1996) in dual image mode to carry out PSF-corrected model fitting photometric analyses of these images. The detection image is a co-add of the i- and z-band images for the tile. Following this approach, we produce an ensemble of several hundred multiband catalogues over the SPT-East region.

In the left-hand panel of Fig. 2, we show the distributions of the 10σ limiting magnitudes measured using the sky noise estimated within 2 arcsec diameter apertures in the co-add images. The $k\sigma$ noise limiting magnitude is defined as

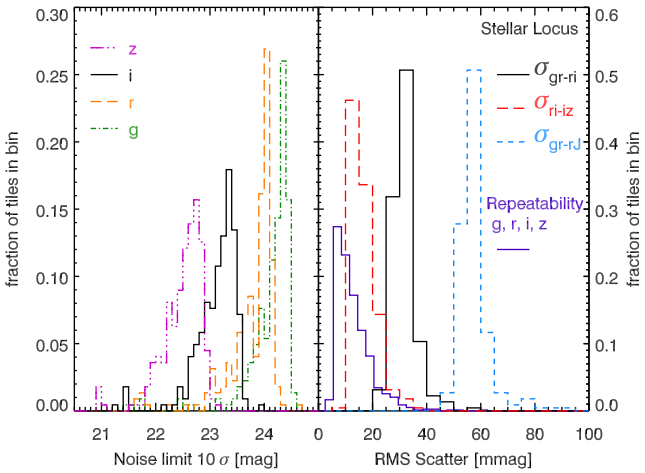

Figure 2. Data quality of the SPT-East region. Left-hand panel: Distribution of 10σ limiting magnitudes of the individual tiles for the *griz* bands. Right-hand panel: Distribution of the stellar locus and repeatability scatter.

$$m_{\mathrm{lim},k\sigma} = Z - 2.5\log_{10} kS_{\mathrm{sky}}, \quad (1)$$

where Z is the zero-point of the stack and S_{sky} is the median absolute deviation of the measured sky background, which is measured from 1000 randomly positioned apertures that exclude object flux. We find the median 10σ limiting magnitudes to be 24.26, 23.97, 23.22, and 22.59 for the *griz* bands of the 223 SPT-East tiles for which such a measurement could be performed. We emphasize that because typically only about 60 per cent of the DES-SV exposures meet the DES imaging requirements (see e.g. Hennig et al. 2017a), that these limiting magnitudes are expected to be ∼0.3 mag shallower than the final DES survey depth.

In the right-hand panel of Fig. 2, the red long-dashed, black solid, and blue short-dashed histograms denote the measured rms scatter around the stellar loci of the same sample of SPT-East co-adds. We show the dispersion in three colour–colour spaces of objects identified as stars, obtained from successive fits of the $g-r$ versus $r-i$, $r-i$ versus $i-z$, and $g-r$ versus $r-J$ colours. The 2MASS J band is added to the fit to calibrate our measurements to an external photometric standard. For details of the methods, we refer the reader elsewhere (Desai et al. 2012; Hennig et al. 2017a). We measure the orthogonal scatter around the stellar loci to be $\sigma_{gr-ri} = 15$ mmag, $\sigma_{ri-iz} = 31$ mmag, and $\sigma_{gr-rJ} = 56$ mmag in very close agreement to the 17, 32, and 57 mmag reported by Hennig et al. (2017a). This performance is significantly better than that achieved within the Sloan Digital Sky Survey (Desai et al. 2012).

Overplotted in the right-hand panel of Fig. 2 as a solid, thick blue line, we present the rms *repeatability scatter* distributions of the SPT-East tiles. This estimator compares measurements of the same source identified in the different overlapping single-epoch images that contribute to the co-add. Hence, it measures the overall photometric stability of the data set, given the underlying instrumental and atmospheric conditions and the robustness of the calibration procedure. Following Desai et al. (2012), we determine the repeatability scatter, which trivially increases towards fainter sources, in magnitude bins, from the brightest photometric bin only, where the photon statistics make a vanishingly small contribution to the scatter. This bin corresponds on average to a magnitude of 15.08 and only includes those tiles (between 185 for the z band to 205 for the r band) that deviate less than 1σ (1.08 mag) from this brightest-bin

magnitude. We find median repeatability scatter of 9.6, 13.7, 13.8, and 11.7 mmag in the *griz* bands, with an overall median of 11.7 mmag. While this repeatability scatter is larger than the ∼8 mmag measured by Hennig et al. (2017a) in DES observations of SPT cluster fields, reflecting the more variable observing depths and conditions, our repeatability scatter is significantly smaller compared to the earlier Blanco Cosmology Survey (Desai et al. 2012) and Pan-STARRS1 (Liu et al. 2015) surveys.

2.2 Galaxy catalogue

In total, we use 225 tiles in the SPT-East region and in total have 208.7 deg^2 of unmasked area. We combine all individual tile catalogues and exclude multiple entries in the overlapping regions. Similarly to Hennig et al. (2017a), we separate galaxies from stars on the bright end by excluding all objects with `spread_model` less than 0.0025. This cut allows a clean separation between galaxies and stars down to $i \sim 22$ mag. Below this magnitude, we attempt no stellar exclusion using object morphology. In this work, we adopt a more conservative limit in i band that is derived for each tile by measuring where the catalogue number density per magnitude starts to continuously fall below a best-fitting power law that was fitted to the region $19 \leq i \leq 21$. Characteristically, this limit lies between $i = 22.2$ and 22.7.

We note that this rather simplistic approach yields conservative limits and can be improved in future work that will involve larger areas or deeper X-ray data. We do not expect that the confirmation of RASS-selected clusters will be limited by the depth of our DES optical data. However, we will return to this issue at a later point of this work.

2.3 The second RASS source catalogue

The second RASS source catalogue (2RXS; Boller et al. 2016) is based on the RASS-3 processed photon event files and uses an improved background determination and detection algorithm, compared to the predecessors: the *ROSAT* bright source catalogue (Voges et al. 1999) and the *ROSAT* faint source catalogue (Voges et al. 2000). The final source catalogue contains about 135 000 detections down to the same detection likelihood as the 1RXS faint source catalogue but without the additional lower limit on source photon counts.

Further, Boller et al. (2016) states that this catalogue is the largest and most reliable all-sky X-ray catalogue available and will likely remain so until the first eROSITA catalogues are created. Thus, the 2RXS catalogue is a well-suited source for testing the optical follow-up of eROSITA cluster candidates and creating cluster catalogues for cosmological studies. Even as the most reliable all-sky X-ray catalogue, Boller et al. (2016) estimates using simulations that the 2RXS contains about 30 per cent spurious detections over the full sky. The fraction of spurious detection shows some dependence on the exposure time and a stronger dependence on likelihood threshold (Boller et al. 2016).

Table 1 in Boller et al. (2016) lists the spurious fraction in bins of existence likelihood for the average survey exposure time and for exposure times above 4000 s. We use this table to assign a probability to be real to each 2RXS source. We find a slightly lower spurious fraction of 22 per cent for the SPT-East region we study in this work. This difference is due to the proximity of the south ecliptic pole and the associated increase in exposure time in RASS, as can be seen in Fig. 1. Although we assume the fraction of spurious sources is strongly suppressed by our optical confirmation tool, we cannot exclude chance superpositions of a spurious X-ray detection with a real optical counterpart.

The 2RXS catalogue further offers measurements on source extent, source variability, and hardness ratio. Due to the large RASS survey PSF with FWHM of ∼4 arcmin (Boese 2000), only a few clusters are reliably estimated as extended. Further, the typically low number of source counts of the majority of the sources do not allow precise measurements of hardness ratios and source variability for those sources. Only 0.4 per cent of the 2RXS sources in our footprint show source variabilities above 3σ. Due to the lack of usefulness of those selection parameters, we decided not to use them and consequently investigate all 2RXS sources for the possibility of being a cluster. From previous RASS-based studies (Henry et al. 2006; Ebeling et al. 2013) and the estimated spurious fraction, we expect only of the order ∼10 per cent of the 2RXS sources to be galaxy clusters. This leads to the fact that cluster confirmation becomes an important factor in this work.

We note that for a potential eROSITA-based survey, the source extent can be used to produce very pure cluster catalogues up to high redshifts prior to the optical follow up, partially reducing the requirements in the optical data to provide photometric redshifts only.

3 CLUSTER CONFIRMATION METHOD

The optical counterparts of X-ray-selected galaxy clusters can be identified in several ways, depending on the availability of optical pass bands and data quality. Methods are based on galaxy clustering, photometric or spectroscopic redshifts or on their appearance in colour–magnitude space. The latter method is called the RS method (Gladders & Yee 2000) and uses the fact that galaxy clusters contain many elliptical galaxies, which are dominated by a stellar population passively evolving since $2 < z < 5$ (e.g. Bower, Lucey & Ellis 1992; Ellis et al. 1997; De Propris et al. 1999; Lin et al. 2006). Those galaxies therefore show a strong 4000 Å break, resulting in a tight colour–magnitude relation for pass bands that include this break at a given redshift. This colour–magnitude relation is called the RS and gives the method its name. We use the RS method together with the galaxy clustering information as the basis for constructing a matched filter for cluster verification and redshift estimation.

Our aim is the identification of X-ray-selected galaxy clusters from the 2RXS catalogue (Boller et al. 2016). We therefore search for cluster candidates in the optical data at the location of every X-ray source that lies in the footprint of our SPT-East data set. In this search, we use the X-ray flux as a redshift-dependent mass constraint, allowing us to identify the physically relevant radius within which to search for optical counterparts. This is done by calculating the cluster richness λ, which is the excess of the weighted sum of galaxies within this radius with respect to the expected number of galaxies in the absence of a cluster. The weights can be seen as filter functions that follow the expected behaviour of cluster galaxies in colour, magnitude and angular space and therefore maximize the chance to detect the cluster at the correct redshift. The final step to quantify the probability of a chance superposition of the X-ray and optical sources involves comparing the measured richness and redshift of the optical counterpart to the distributions of richness and redshift determined along random lines of sight, where there is no 2RXS detection but similar X-ray exposure time.

The details of the different components of this multicomponent matched filter (MCMF) cluster confirmation tool are explained in the following subsections.

Table 1. List of all 2RXS clusters with at least one peak in redshift exceeding P_λ and $P_s > 0.98$ and $P_* < 0.1$. Multiple X-ray associations with the same optical cluster are excluded. Only the parameters related to the two peaks with highest value in P_λ are shown.

Name	RA	DEC.	$P_{\lambda 1}$	$P_{\lambda 2}$	P_{s1}	P_{s2}	P_*	z_1	z_2	$\sigma_{z,1}$	$\sigma_{z,2}$	λ_{MCMF1}	λ_{MCMF2}	$\sigma_{\lambda 1}$	$\sigma_{\lambda 2}$
2RXC J0418.3-5850	64.6230	−58.8490	0.988	0.938	0.986	0.531	0.00	0.278	1.017	0.013	0.020	34.8	70.3	6.3	45.3
2RXC J0420.6-5246	65.2350	−52.7810	0.991	0.593	0.991	0.540	0.00	0.318	0.596	0.013	0.016	58.4	14.9	8.2	6.6
2RXC J0423.5-5432	65.9700	−54.5460	1.000	0.951	1.000	0.946	0.00	0.255	0.428	0.013	0.014	73.4	30.8	9.1	6.3
2RXC J0424.3-5557	66.1130	−55.9550	0.995	0.685	0.995	0.683	0.00	0.226	0.458	0.012	0.015	41.6	13.3	6.8	4.7
2RXC J0425.4-6143	66.4340	−61.7310	1.000	0.000	1.000	0.000	0.00	0.704	–	0.017	–	132.5	–	14.7	–
2RXC J0426.2-5517	66.5980	−55.3000	0.990	0.723	0.984	0.774	0.00	0.417	0.053	0.014	0.011	59.6	5.3	8.6	2.3
2RXC J0426.4-4545	66.6830	−45.7570	1.000	0.000	1.000	0.000	0.00	0.281	–	0.013	–	51.8	–	7.8	–
2RXC J0426.5-6003	66.6960	−60.0500	0.986	0.315	0.981	0.338	0.00	0.064	0.461	0.011	0.015	14.0	6.2	4.0	3.5
2RXC J0428.4-5349	67.1750	−53.8280	0.993	0.950	0.993	0.965	0.00	0.261	0.048	0.013	0.010	61.4	16.2	8.4	4.1
2RXC J0428.6-6019	67.2480	−60.3210	1.000	0.664	1.000	0.678	0.00	0.219	0.531	0.012	0.015	71.1	13.0	8.6	5.1
2RXC J0429.1-6020	67.3120	−60.3490	1.000	0.425	1.000	0.439	0.00	0.223	0.531	0.012	0.015	51.6	9.1	7.4	4.5
2RXC J0430.2-6127	67.5820	−61.4530	1.000	0.977	1.000	0.985	0.00	0.076	0.771	0.011	0.018	54.9	76.5	7.6	14.7
2RXC J0430.4-5336	67.6660	−53.6150	1.000	0.900	1.000	0.749	0.00	0.045	0.991	0.010	0.020	34.6	76.3	6.2	39.9
2RXC J0430.5-5737	67.7010	−57.6250	0.995	0.076	0.993	0.066	0.00	0.284	0.077	0.013	0.011	50.0	0.6	7.6	1.2
2RXC J0431.1-6246	67.8060	−62.7710	0.991	0.505	0.993	0.573	0.00	0.224	0.057	0.012	0.011	37.6	2.6	6.3	1.6
2RXC J0431.1-6033	67.8090	−60.5550	0.998	0.755	0.998	0.947	0.00	0.613	0.894	0.016	0.019	56.9	25.6	8.6	8.3
2RXC J0431.3-6126	67.8650	−61.4350	1.000	0.928	1.000	0.903	0.00	0.077	0.129	0.011	0.011	93.2	18.5	10.1	5.4
2RXC J0432.2-5942	68.0650	−59.7040	0.984	0.552	0.990	0.562	0.00	0.156	0.291	0.012	0.013	19.8	6.3	4.6	3.1
2RXC J0432.6-4549	68.2430	−45.8330	1.000	0.770	1.000	0.794	0.00	0.248	0.136	0.012	0.011	72.9	7.5	9.1	2.9
2RXC J0433.3-5511	68.3580	−55.1870	0.995	0.549	0.995	0.575	0.00	0.690	0.496	0.017	0.015	63.9	10.9	10.6	4.4
2RXC J0434.1-4551	68.5280	−45.8530	0.987	0.000	0.985	0.000	0.00	0.162	–	0.012	–	20.9	–	4.9	–
2RXC J0434.1-4943	68.5440	−49.7310	1.000	0.532	1.000	0.792	0.00	0.244	0.033	0.012	0.010	48.4	2.0	7.0	1.0
2RXC J0434.6-4726	68.7290	−47.4430	1.000	0.102	0.998	0.066	0.00	0.310	0.077	0.013	0.011	67.9	1.0	9.1	1.9
2RXC J0435.4-5801	68.9090	−58.0220	0.989	0.813	0.989	0.763	0.00	0.222	0.457	0.012	0.015	41.1	19.8	6.9	6.1
2RXC J0435.5-4540	68.9560	−45.6710	0.998	0.153	0.998	0.167	0.00	0.167	0.027	0.012	0.010	51.0	0.8	7.6	1.0
2RXC J0436.3-6032	69.1270	−60.5380	0.996	0.762	0.996	0.932	0.00	0.476	0.781	0.015	0.018	47.0	20.0	7.3	6.5
2RXC J0437.1-4731	69.3000	−47.5280	0.990	0.622	0.990	0.654	0.00	0.297	0.179	0.013	0.012	62.4	10.0	8.8	3.9
2RXC J0437.3-5753	69.3620	−57.8910	1.000	0.897	0.995	0.892	0.00	0.379	0.598	0.014	0.016	60.3	25.9	8.4	7.0
2RXC J0438.1-4559	69.5210	−45.9840	0.997	0.000	0.992	0.000	0.00	0.154	–	0.012	–	33.6	–	6.5	–
2RXC J0438.1-4858	69.5220	−48.9770	0.991	0.470	0.989	0.495	0.00	0.224	0.544	0.012	0.015	33.4	8.9	6.2	4.2
2RXC J0438.2-5419	69.5650	−54.3270	1.000	0.707	1.000	0.733	0.00	0.424	0.575	0.014	0.016	120.7	24.5	11.9	7.8
2RXC J0438.2-4555	69.5910	−45.9210	0.995	0.415	0.987	0.185	0.00	0.151	1.006	0.012	0.020	23.9	22.9	5.8	21.1
2RXC J0438.3-4906	69.6170	−49.1090	0.998	0.000	0.998	0.000	0.00	0.247	–	0.012	–	86.5	–	10.0	–
2RXC J0439.1-4600	69.8060	−46.0140	0.993	0.560	0.986	0.619	0.00	0.344	0.128	0.013	0.011	77.1	6.5	10.0	3.0
2RXC J0439.6-4842	70.0000	−48.7120	1.000	0.347	1.000	0.611	0.00	0.256	0.040	0.013	0.010	58.3	1.5	7.9	1.0
2RXC J0440.5-4657	70.2080	−46.9630	1.000	0.752	1.000	0.667	0.00	0.329	0.570	0.013	0.016	104.0	19.3	10.1	7.0
2RXC J0440.5-4743	70.2180	−47.7210	1.000	0.107	1.000	0.059	0.00	0.310	0.567	0.013	0.016	193.2	5.2	10.8	6.0
2RXC J0440.6-4510	70.2480	−45.1710	1.000	0.408	0.997	0.405	0.00	0.158	0.703	0.012	0.017	42.4	12.7	7.2	7.4
2RXC J0441.0-4830	70.2620	−48.5070	1.000	0.508	1.000	0.508	0.00	0.249	0.121	0.012	0.011	82.2	4.8	9.7	2.6
2RXC J0441.1-4502	70.3080	−45.0490	0.998	0.825	0.998	0.614	0.00	0.165	0.968	0.012	0.020	42.3	45.5	7.2	29.7
2RXC J0446.1-5142	71.5330	−51.7130	0.998	0.504	0.998	0.485	0.00	0.464	0.312	0.015	0.013	81.4	9.8	10.2	4.5
2RXC J0446.6-4834	71.7390	−48.5680	0.993	0.464	0.988	0.451	0.00	0.760	1.024	0.018	0.020	73.3	26.1	13.9	19.0
2RXC J0447.2-5055	71.8510	−50.9230	1.000	0.599	1.000	0.647	0.00	0.402	0.235	0.014	0.012	84.4	7.3	9.6	3.2
2RXC J0447.3-5145	71.8910	−51.7540	1.000	0.912	1.000	0.902	0.00	0.415	0.556	0.014	0.016	67.9	22.9	8.7	6.2
2RXC J0447.5-5045	71.9410	−50.7570	1.000	0.554	1.000	0.515	0.00	0.580	0.795	0.016	0.018	66.3	15.7	9.5	9.3
2RXC J0448.3-4540	72.1250	−45.6700	0.995	0.889	0.995	0.971	0.00	0.300	0.535	0.013	0.015	58.4	26.5	8.3	5.2
2RXC J0449.1-4900	72.2960	−49.0120	1.000	0.257	1.000	0.323	0.00	0.791	0.235	0.018	0.012	184.5	3.5	22.8	2.3
2RXC J0449.2-4815	72.3490	−48.2650	0.982	0.185	0.988	0.109	0.00	0.578	0.727	0.016	0.017	37.7	7.1	7.1	6.6
2RXC J0449.3-5407	72.3560	−54.1260	0.991	0.937	0.991	0.912	0.00	0.629	0.209	0.016	0.012	51.5	15.5	8.7	4.6
2RXC J0449.6-4440	72.4800	−44.6790	1.000	0.484	1.000	0.378	0.00	0.159	0.605	0.012	0.016	88.1	17.7	9.9	8.7
2RXC J0451.5-5058	72.9620	−50.9710	1.000	0.717	0.998	0.720	0.00	0.761	0.398	0.018	0.014	105.5	12.6	14.7	4.3
2RXC J0451.5-4521	72.9690	−45.3550	0.984	0.828	0.984	0.817	0.00	0.227	0.497	0.012	0.015	30.8	18.4	5.8	5.4
2RXC J0500.5-5115	75.2290	−51.2620	1.000	0.000	1.000	0.000	0.00	0.158	–	0.012	–	72.2	–	8.8	–
2RXC J0500.6-6346	75.2420	−63.7670	0.981	0.000	0.983	0.000	0.00	0.390	–	0.014	–	35.0	–	6.2	–
2RXC J0503.4-5658	75.9030	−56.9750	1.000	0.649	1.000	0.704	0.00	0.134	0.433	0.011	0.014	45.5	13.6	6.7	4.5
2RXC J0504.0-4929	76.0100	−49.4900	0.995	0.579	0.991	0.678	0.00	0.218	0.364	0.012	0.014	47.9	10.1	7.6	3.7
2RXC J0505.3-6145	76.3610	−61.7500	1.000	0.287	1.000	0.200	0.00	0.262	0.734	0.013	0.017	90.8	11.0	9.7	8.5
2RXC J0506.1-6310	76.5260	−63.1700	1.000	0.923	1.000	0.907	0.00	0.293	0.171	0.013	0.012	72.5	13.6	8.6	4.2
2RXC J0509.3-5640	77.3690	−56.6740	0.989	0.605	0.996	0.603	0.00	0.595	0.279	0.016	0.013	49.8	7.8	8.4	3.5
2RXC J0510.0-6118	77.5050	−61.3050	1.000	0.572	1.000	0.667	0.00	0.388	0.503	0.014	0.015	110.2	11.2	10.5	4.2
2RXC J0515.1-6159	78.8030	−61.9950	0.994	0.904	0.994	0.891	0.00	0.126	0.230	0.011	0.012	27.3	19.2	5.6	5.2
2RXC J0516.3-5431	79.1450	−54.5180	1.000	0.127	1.000	0.146	0.00	0.300	0.010	0.013	0.010	158.7	0.6	13.1	1.0
2RXC J0517.4-5602	79.4140	−56.0410	0.993	0.792	0.988	0.805	0.00	0.178	0.090	0.012	0.011	28.8	6.7	6.0	2.7

Table 1 – *continued*

Name	RA	DEC.	$P_{\lambda 1}$	$P_{\lambda 2}$	P_{s1}	P_{s2}	P_*	z_1	z_2	$\sigma_{z,1}$	$\sigma_{z,2}$	λ_{MCMF1}	λ_{MCMF2}	$\sigma_{\lambda 1}$	$\sigma_{\lambda 2}$
2RXC J0517.6-5834	79.4890	−58.5740	1.000	0.754	1.000	0.397	0.00	0.111	0.120	0.011	0.011	42.2	9.7	6.6	6.2
2RXC J0518.2-5601	79.6020	−56.0190	1.000	0.477	1.000	0.609	0.00	0.351	0.515	0.014	0.015	64.6	8.5	8.4	3.6
2RXC J0518.3-5616	79.6170	−56.2700	0.994	0.000	0.990	0.000	0.00	0.123	–	0.011	–	25.7	–	5.4	–
2RXC J0518.5-5720	79.6910	−57.3450	0.998	0.341	1.000	0.211	0.00	0.290	0.949	0.013	0.019	60.5	19.0	8.1	16.9
2RXC J0519.2-6109	79.8430	−61.1510	0.986	0.000	0.989	0.000	0.00	0.102	–	0.011	–	22.5	–	4.8	–
2RXC J0524.5-5550	81.1990	−55.8420	0.983	0.383	0.983	0.492	0.00	0.200	0.391	0.012	0.014	36.0	7.9	6.6	3.5
2RXC J0524.6-5814	81.2430	−58.2380	1.000	0.082	1.000	0.082	0.00	0.310	0.741	0.013	0.017	100.6	5.2	10.4	6.3
2RXC J0525.6-6212	81.4800	−62.2110	1.000	0.189	1.000	0.176	0.00	0.150	0.556	0.011	0.016	31.3	5.5	5.9	4.3
2RXC J0528.4-6218	82.1720	−62.3080	0.997	0.000	0.997	0.000	0.00	0.117	–	0.011	–	22.1	–	4.9	–
2RXC J0528.6-6214	82.2420	−62.2420	0.985	0.068	0.991	0.082	0.00	0.129	0.235	0.011	0.012	16.4	1.3	4.1	2.0
2RXC J0534.3-6238	83.6320	−62.6490	1.000	0.124	1.000	0.032	0.00	0.128	0.131	0.011	0.011	28.7	1.4	5.4	5.4
2RXC J0536.2-5847	84.0960	−58.7860	0.996	0.538	0.994	0.540	0.00	0.394	0.706	0.014	0.017	48.2	12.3	7.3	6.5
2RXC J0536.4-6251	84.1590	−62.8570	1.000	0.857	1.000	0.901	0.00	0.178	0.084	0.012	0.011	34.3	7.6	6.2	2.6
2RXC J0538.3-6031	84.6190	−60.5260	0.994	0.962	0.989	0.127	0.00	0.400	1.064	0.014	0.021	43.9	86.3	7.0	80.4
2RXC J0538.4-6046	84.6460	−60.7720	0.988	0.434	0.986	0.217	0.87	0.548	0.826	0.015	0.018	43.2	13.0	8.2	11.3
2RXC J0540.5-6144	85.2200	−61.7380	1.000	0.000	1.000	0.000	0.00	0.124	–	0.011	–	51.7	–	7.4	–
2RXC J0541.0-6251	85.2530	−62.8670	1.000	0.087	1.000	0.082	0.00	0.123	0.810	0.011	0.018	39.8	7.3	6.2	8.4
2RXC J0541.1-6414	85.2860	−64.2340	0.991	0.226	0.989	0.307	0.00	0.393	0.542	0.014	0.015	42.7	5.8	6.9	3.5
2RXC J0541.2-6254	85.3350	−62.9150	0.997	0.000	0.997	0.000	0.14	0.110	–	0.011	–	23.5	–	4.9	–
2RXC J0542.4-6154	85.6510	−61.9040	1.000	0.167	1.000	0.167	0.00	0.124	0.367	0.011	0.014	57.3	5.5	7.6	4.1
2RXC J0543.0-6219	85.7650	−62.3200	1.000	0.646	1.000	0.681	0.00	0.468	0.064	0.015	0.011	75.5	3.7	9.1	2.1
2RXC J0549.2-6205	87.3300	−62.0870	1.000	0.772	1.000	0.717	0.00	0.413	0.135	0.014	0.011	201.5	10.7	15.1	4.3
2RXC J0552.0-6243	88.0050	−62.7200	0.990	0.928	0.983	0.903	0.00	0.152	0.417	0.012	0.014	21.4	23.7	5.3	5.9
2RXC J0552.3-6427	88.1120	−64.4670	1.000	0.533	1.000	0.572	0.00	0.424	0.261	0.014	0.013	65.9	5.6	8.9	2.8
2RXC J0555.3-6406	88.8670	−64.1050	1.000	0.970	1.000	0.970	0.00	0.391	0.205	0.014	0.012	150.7	26.7	12.7	5.6
2RXC J0602.1-6445	90.5350	−64.7560	0.987	0.499	0.987	0.618	0.00	0.069	0.422	0.011	0.014	13.9	8.2	3.7	3.2

3.1 X-ray luminosity

To define the region in which we are searching for counterparts, we need to estimate the X-ray luminosity under the assumption that the observed X-ray source is a galaxy cluster. The basis of the X-ray luminosity estimate for each source is the X-ray count rate in the 2RXS catalogue. The count rate is obtained within a minimum aperture of 5 arcmin radius around each 2RXS position. If the extent of the source is found to be larger than this, the extraction radius is increased. In the SPT-East region, all but two of the sources have extraction radii equal to this minimum value.

Because fits to the X-ray spectra are only possible for a tiny fraction of the sources, we have to assume a spectral model with given temperature to obtain luminosities from the 2RXS catalogue. We can convert the X-ray count rate to an X-ray luminosity in the 0.1–2.4 keV band using an APEC plasma model (Smith et al. 2001) of a certain temperature and metal abundance, a specific redshift and the appropriate neutral hydrogen column density. We create for this task a look-up table for different redshifts, metal abundance, plasma temperatures, and neutral hydrogen column densities.

For this work, we fix temperature and metal abundance to 5 keV and 0.4 solar metallicity, respectively. We further assume that our fiducial luminosity L_X corresponds closely to L_{500}, the luminosity in the 0.1–2.4 keV band within a radius within which the mean density is 500 times the critical density at the assumed cluster redshift. Although our fiducial luminosity is derived from count rates within a fixed aperture, we do not expect this inconsistency to be an important source of scatter, given the large intrinsic scatter in the cluster L_X–mass relation. It would result in a mass and redshift-dependent bias. Assuming the X-ray surface brightness profile following a beta profile with $\beta \approx 2/3$, the flux differs less than 6 per cent for radii between 0.65 and 2 times r_{500} from the value at r_{500}. Such a small bias is not important for the analysis presented here. A more sophisticated iterative approach using a luminosity–temperature relation is planned in combination with re-centring and re-extraction of the X-ray count rate for the upcoming full DES analysis of the 2RXS catalogue. All luminosities are presented in units of 10^{44} erg s^{-1}.

3.2 Cluster mass and follow-up region of interest

We measure the cluster matched filter richness λ_{MCMF} as a function of redshift along the line of sight towards each X-ray-selected candidate. λ_{MCMF} is extracted within a radius r_{500}. We derive this radius using the estimated luminosity at that redshift and a L_X–mass scaling relation. For this analysis, we use the RASS-based scaling relation given in Mantz et al. (2010b), which has the form

$$\langle \ell(m) \rangle = \beta_0 + \beta_1 m. \tag{2}$$

With the terms

$$\ell = \log_{10}\left(\frac{L_X}{E(z)10^{44}\,\mathrm{erg\,s^{-1}}}\right),$$
$$m = \log_{10}\left(\frac{E(z)M_{500}}{10^{15}\,\mathrm{M_\odot}}\right), \tag{3}$$

which include factors of the normalized Hubble parameter, $E(z) = H(z)/H_0$. As scaling parameter β_0 and β_1, we take 0.8 and 1.34 (as given in table 7 of Mantz et al. 2010b), assuming our fiducial X-ray luminosity is a reasonable estimate of L_{500}. The exact choice of the scaling relation used at this stage of the project is not crucial, because we are mainly using these mass estimates to determine the region of interest within which we search for optical counterparts. The region of interest, r_{500}, is finally derived from M_{500} using our fiducial cosmology and the redshift. The usage of r_{500} from the X-ray as the extraction radius allows us to limit the impact of projection effects on our measurement and makes use of

the mass information available in the X-ray catalogue. We note that depending on the characteristics of the survey to be followed up using MCMF (e.g. positional accuracy), the optimal choice of the extraction radius may differ.

3.3 Radial filter

To use the clustering information in our code, we apply a radial weighting $\Sigma(R)$ based on a Navarro, Frenk and White (NFW) profile (Navarro, Frenk & White 1997). The corresponding projected NFW that we use as a spatial weighting function is (Bartelmann 1996)

$$\Sigma(R) \propto \frac{1}{(R/R_s)^2 - 1} f(R/R_s), \tag{4}$$

where R_s is the characteristic scale radius, and

$$f(x) = \begin{cases} 1 - \frac{2}{\sqrt{x^2-1}} \arctan \sqrt{\frac{x-1}{x+1}} & (x > 1) \\ 1 - \frac{2}{\sqrt{1-x^2}} \arctan \mathrm{h} \sqrt{\frac{1-x}{x+1}} & (x < 1). \end{cases} \tag{5}$$

We use a scale radius $\mathrm{R_s} = R_{500}/3$, which is consistent with the typical concentration of RS galaxies found in massive clusters extending to redshift $z \sim 1$ (Hennig et al. 2017a). We adopt a minimum radius of 0.1 h^{-1} Mpc, below which we set the radial weight to be constant (Rykoff et al. 2014).

The profile $\Sigma(R)$ is truncated at the cluster radius $R_{500}(z)$, and the correction term $C_{\rm rad}$ is chosen such that the radial filter is normalized as

$$1 = C_{\rm rad} \int_0^{R_{500}(z)} \mathrm{d}R\, 2\pi R \Sigma(R). \tag{6}$$

The radial weight assigned to a galaxy i at a given radial distance R_i from the assumed centre is then simply,

$$n_i(z) = C_{\rm rad}(z) 2\pi R_i \Sigma(R_i). \tag{7}$$

Rykoff et al. (2012) showed that their matched filter richness is only weakly dependent on the shape of the radial filter. They found that the ratio of the intrinsic scatter of the L_X–λ relation using a flat radial weight over that using an NFW-based radial filter is only $\sigma_{L_X|\lambda_{\rm flat}}/\sigma_{L_X|\lambda_{\rm NFW}} = 1.03 \pm 0.015$. The precise choice of the parameter values entering the NFW profile are therefore likely of low relevance and will be explored in future work, once a larger cluster sample is available.

3.4 Colour–magnitude filter

To obtain a clean selection of RS galaxies, we use information from all the available bands rather than only using the bands that bracket the 4000 Å break. The basic requirement, then, is that a cluster galaxy candidate has to be consistent with a passively evolving galaxy in all colours, even if there is no tight RS visible at a given redshift and colour.

As a baseline RS model, we use the same models as described in Hennig et al. (2017b). Those models have been used for a DES study of galaxy populations of massive, Sunyaev–Zel'dovich effect (SZE) selected clusters up to a redshift of 1.1 (see also Zenteno et al. 2011; Song et al. 2012; Liu et al. 2015; Zenteno et al. 2016). Because the models are meant to describe the RS in colour–magnitude space, where the filter combination includes the 4000 Å break and the next reddest band, it is not guaranteed that the model performs well for other filter combinations. We therefore use two galaxy cluster subsamples from the SPT survey with spectroscopic cluster redshifts (Ruel et al. 2014; Bayliss et al. 2016) to calibrate the RS models and estimate the width of the RS for a given redshift and colour. In this tuning process, we keep the slope fixed to that from the model and just allow the normalization to vary. Furthermore, we estimate the total scatter (observational plus intrinsic) of the RS in each colour. Ultimately, we may return to the underlying RS model and tune it in a less ad hoc manner once we extend the analysis to the full DES data set.

We define all galaxies that lie within three times the standard deviation from the RS model in colour–magnitude space in all of the following colour combinations $(c_1, c_2, c_3) = (g-r, r-i, i-z)$ to be candidate cluster members. We weight each cluster galaxy candidate i with a redshift z-dependent value

$$w_i(z) = \frac{\prod_{j=1}^{3} G\left(c_{i,j} - \langle c(z)\rangle_j, \sigma_{c_j}(z)\right)}{N(\sigma_{c_1}(z), \sigma_{c_2}(z), \sigma_{c_3}(z))}, \tag{8}$$

where $G\left(\Delta c_{i,j}, \sigma_{c_j}(z)\right)$ is the value of a normalized Gaussian function at colour offset $\Delta c_{i,j} = c_{i,j} - \langle c(z)\rangle_j$, where for band j and redshift z the expected RS colour and measurement standard deviation are $\langle c(z)\rangle_j$ and $\sigma_{c_j}(z)$, respectively. We normalize the weights by $N(\sigma_{c_1}(z), \sigma_{c_2}(z), \sigma_{c_3}(z))$, which is the average weight of a population of galaxies that follows the expected distribution of a cluster at the investigated redshift.

3.5 Luminosity cut and incompleteness correction

We do not apply a luminosity-based weight to the galaxies, but we limit the number of galaxies investigated at a given redshift by selecting only galaxies that are brighter than $i \leqq m^*(z) + 1.25$, where $m^*(z)$ is the expected characteristic magnitude for a cluster at redshift z. This magnitude cut-off can exceed the completeness limit $c_{\rm lim}$ of the data at higher redshift in some locations within the SPT-East region. These clusters would be still detectable, but the estimated richness would be biased low. We account for this effect by rescaling the measured richness to $c_{\rm lim}$ by using the correction factor

$$C_{\rm cmp} = \frac{\int_{m^*(z)-4.6}^{m^*(z)+1.25} S(m^*(z), m, \alpha)\mathrm{d}m}{\int_{m^*(z)-4.6}^{c_{\rm lim}} S(m^*(z), m, \alpha)\mathrm{d}m}, \tag{9}$$

where $S(m^*(z), m, \alpha)$ is the Schechter function (Schechter 1976), in which $m^*(z)$ is the characteristic magnitude expected at redshift z. The faint end slope α is set to $\alpha = -1$ in our analysis, but it can be adjusted with redshift and mass to match any measured trends (e.g. Zenteno et al. 2016). Assuming the galaxy population follows the Schechter function, equation (9) gives the fraction of galaxies brighter than the completeness limit compared to the number of galaxies that would be brighter than $m^*(z) + 1.25$. When $m*(z) + 1.25 < c_{\rm lim}$ we set $C_{\rm cmp} = 1$.

3.6 Masking and background estimation

At each RASS position, we select all sources within a distance of 0.5 deg. We create a smoothed source density map with a pixel scale of 2 arcsec, using a box-car smoothing with box size that contains on average 16 sources. We use square and rectangular boxes to further improve the detection and the modelling of masked regions.

This robustly masks regions around very bright sources, accounting for the complex edges of the DES-SV area and non-uniformities in the shapes of very bright sources. The number of unmasked pixels gives the available area for the background and cluster counts.

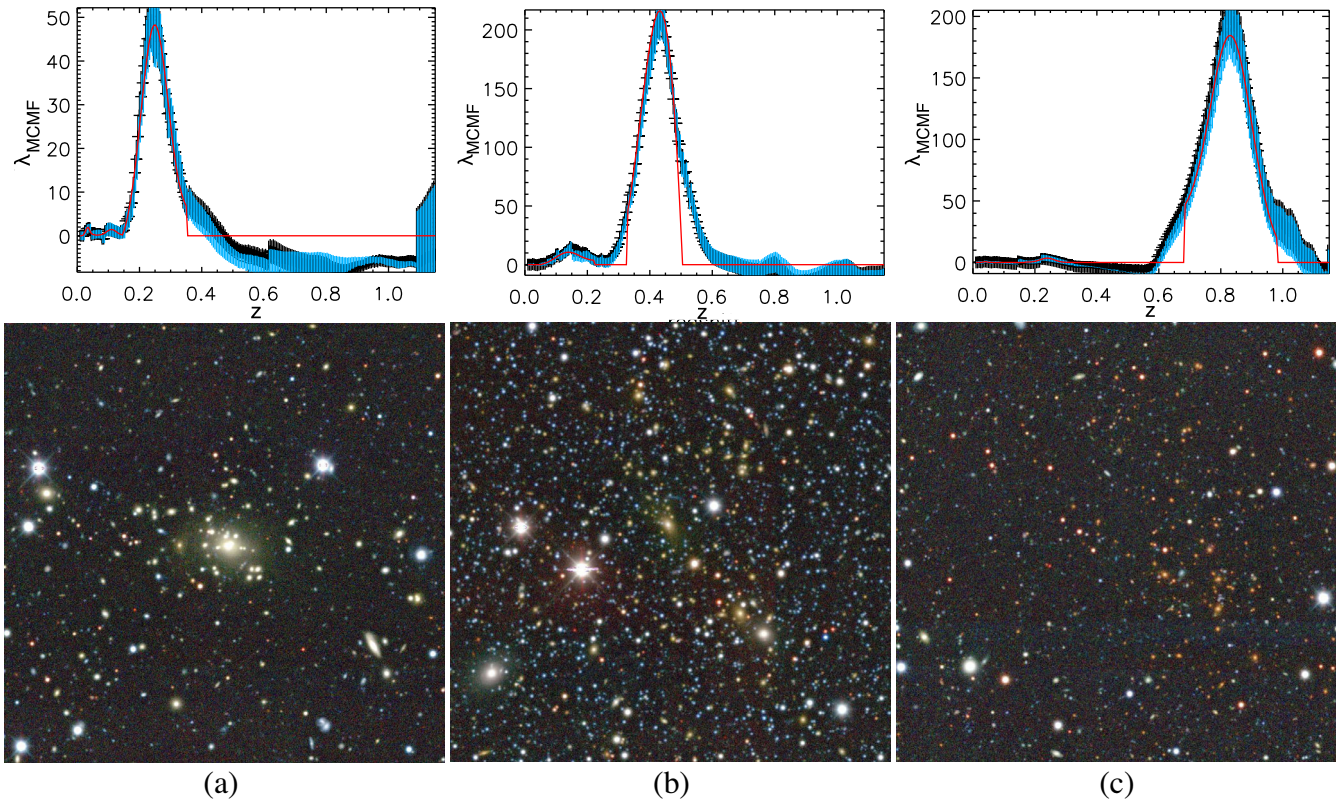

Figure 3. Three RASS galaxy clusters identified in the DES-SV region. Top panel: richness versus redshift plot with Gaussian fit to the most significant peaks. Black points are based on global background estimation, blue points show the results based on the local background estimation. Bottom panel: optical *grz* pseudo-colour images of the central 5 × 5 arcmin regions around each of the RASS position. The corrected redshifts found for these clusters are $z = 0.22$ (a), 0.40 (b) and 0.77 (c).

These mask images are also used to adapt the normalization of the radial weight, accounting for masked regions.

We use two different approaches to estimate the background correction for a cluster at a given redshift. The global background approach uses a merged source catalogue of tiles with similar or higher completeness limits than that estimated locally. This approach takes advantage of the increased statistics that comes with larger area but is also not sensitive to variations in local image properties such as image depth variation or stellar density. The local background approach uses all sources within the range $r_{500} < r < 0.5$ deg. This follows the local conditions more closely, which becomes increasingly important at the higher redshifts probed by our method.

3.7 Identifying cluster candidates and estimating redshifts

We define our filtered richness $\lambda_{\rm MCMF}$ as

$$\lambda_{\rm MCMF}(z) = \frac{C_{\rm cmp}(z)A_{\rm tcl}(z)}{A_{\rm cl}(z)}\left(\sum_i w_i(z)n_i(z) - \frac{A_{\rm cl}(z)}{A_{\rm BG}(z)}\sum_j w_j(z)\right), \quad (10)$$

the sum of the colour and the radial weight over all cluster candidates minus the scaled background, where j runs over all background galaxies that fulfil the same colour and magnitude cuts as for the cluster candidates. Here, the elements $A_{\rm cl}$ and $A_{\rm BG}$ correspond to the unmasked cluster and background area and $A_{\rm tcl}$ to the total area within $r_{500}(z)$. $\lambda_{\rm MCMF}$ is calculated for redshifts between $0.01 < z < 1.15$ in steps of $\delta z = 0.005$. For each $\lambda_{\rm MCMF}$ estimate, we calculate the uncertainty $\Delta\lambda_{\rm MCMF}$ assuming Poisson statistics as

$$\Delta\lambda_{\rm MCMF}(z) = \frac{C_{\rm cmp}(z)A_{\rm tcl}(z)}{A_{\rm cl}(z)}\left(\sum_i w_i(z)n_i(z) + \left(\frac{A_{\rm cl}(z)}{A_{\rm BG}(z)}\right)^2\sum_j w_j(z)\right)^{0.5}. \quad (11)$$

We call the ratio of the $\lambda_{\rm MCMF}$ measurement to the Poisson uncertainty the signal-to-noise ratio $S = \lambda_{\rm MCMF}/\Delta\lambda_{\rm MCMF}$ of the detection.

The distribution of $\lambda_{\rm MCMF}$ versus redshift is searched for up to five peaks. These peaks are then subsequently fitted with Gaussian functions, and the three most significant peaks are kept for further analysis. To improve the robustness of the fits and to avoid confusion with multiple peaks, we limit the fitting range around each peak that we find. Depending on the initial guess for the peak position, we limit the fitting range to be $|z - z_{\rm peak}| < 0.08$ for $z_{\rm peak} < 0.2$, $|z - z_{\rm peak}| < 0.10$ for $z_{\rm peak} < 0.4$, and $|z - z_{\rm peak}| < 0.15$ for $z_{\rm peak} > 0.4$. The best fit provides the richness and redshift estimate for each peak. No deblending of nearby peaks is performed. The search for peaks is performed for the global and the local background approach independently; however, we generally use the local approach for redshifts above $z = 0.15$ and the global approach at lower redshifts. Fig. 3 shows three examples of clusters identified with MCMF, and Fig. 4 shows an example of an RASS candidate with multiple optical counterpart peaks along the line of sight.

To obtain optical positions for each of the identified peaks, a weighted galaxy density map is created by using a Voronoi Tessellation method and then smoothed with a Gaussian kernel of

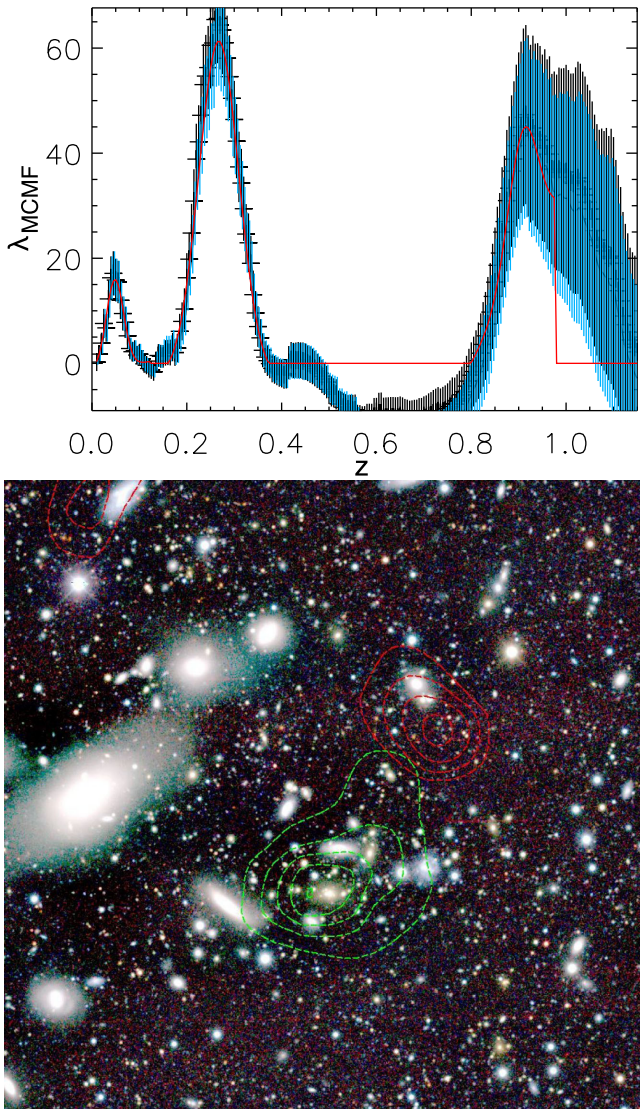

Figure 4. RASS position with three significant peaks in redshift at $z = 0.05$, 0.24 and 0.87. The top panel shows the richness versus redshift plot, with Gaussian fits to the three peaks. Masking by the two clusters at lower redshifts results in an apparent under density at redshifts $z > 0.5$. Bottom panel: *grz* pseudo-colour image of the 10×10 arcmin region around the RASS position. Contours show the galaxy number density corresponding to the two redshift peaks with $z > 0.2$ identified in the upper panel.

250 kpc size. The weighting is performed by using the derived colour weights from the richness estimator at the redshift of the identified peak. This efficiently suppresses the signal from structures at other redshifts and reduces the median offset between SPT centres and galaxy density centres by 0.1 arcmin or 16 per cent compared to the unweighted estimates (for discussion of offsets between SPT and optical positions, see Song et al. 2012; Saro et al. 2015). Finally, we use `SExtractor` (Bertin & Arnouts 1996) to identify the galaxy density peak that lies nearest the X-ray candidate position.

3.8 Quantifying probability of random superposition

To estimate the chance of random superpositions of unrelated optical clusters on to lines of sight corresponding to X-ray sources, we apply our method to random positions in the survey field (see also Saro et al. 2015). In this estimate, we exclude 6 arcmin radius regions around the 2RXS X-ray positions and exclude also regions with low-RASS exposure times. The lower exposure time cut ensures that the median X-ray exposure time in the region where random lines of sight are evaluated is similar to that in the region where the 2RXS follow-up is carried out. For this analysis, we use 2587 random positions, and we run our code using X-ray count rates corresponding to the 25, 50, 75, and 95 percentiles of the count rate distribution of RASS sources that overlap the SPT-East region.

Then, for each peak found at an RASS position, we calculate the fraction P_λ of sources in the random catalogue with $|z_{\rm RASS} - z_{\rm rand}| < 0.075$ that have richnesses equal to or below the richness found for the RASS cluster candidate. Because the aperture of the cluster finder is based on the X-ray count rate, we use the random catalogue where the count rate is closest to that of the RASS cluster candidate. This fraction corresponds to the probability that the optical cluster counterpart identified for a particular RASS source at a given redshift and mass is real as opposed to a random superposition of an unassociated optical system.

As an alternative approach, we also estimate the fraction $P_{\rm s}$ of sources in the random catalogue with $|z_{\rm RASS} - z_{\rm rand}| < 0.075$ that have a signal-to-noise ratio S equal to or below that found for the RASS cluster candidate. This estimator accounts for the local variations in imaging depth as well as the effects of masking, but at the price of partially loosening the correlation between X-ray detection probability, mass and redshift.

4 APPLICATION TO RASS AND DES-SV DATA SETS

We test our method by applying it to the RASS and DES-SV data sets described in Section 2. Below we first discuss the performance of the cluster matched filter in the face of stellar contamination (Section 4.1). Then in Section 4.2, we present the cluster sample and examine its characteristics, including the photometric redshift accuracy, the optical–X-ray scaling relations and the centre offset distributions. Finally, in Section 4.3, we compare our cluster sample to three other samples extracted over the same sky area.

4.1 Sensitivity to stellar contamination

Stars can interfere with our follow-up of galaxy clusters if they slip through our cluster filter, creating fake signals, affecting galaxy colours by reflected light or being X-ray emitters by themselves. In this section, we address these issues by performing two tests. The cluster confirmation method we present will be applied over a large area and therefore has to be robust against large changes in the stellar density. The changes in stellar density are especially large in the DES-SV region, due to its proximity to the Magellanic clouds. Our data set is therefore well suited for these tests.

4.1.1 Stars and star clusters

The first test uses a catalogue of only stars and measures what fraction of the input signal makes it through our cluster filter. To obtain a clean star catalogue, we use the DECam observations of the COSMOS field and match the detected sources with stars from the COSMOS photo-z catalogue (Ilbert et al. 2009). No radial filtering or weighting is used in the test. Rather, the input catalogue is filtered by colour and magnitude, and as a last step the cut in

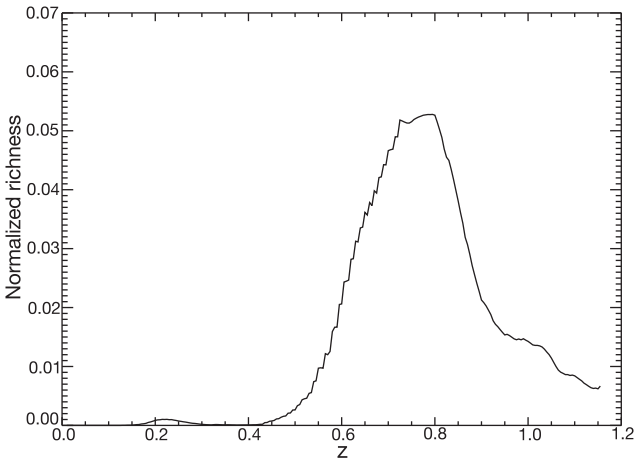

Figure 5. The fraction of stars leaking into the galaxy sample for a completeness limit of $i = 22.5$ mag. A maximum of 5 per cent of the input signal is reached at a redshift of $z = 0.75$.

`spread_model` is applied. The output signal is normalized to the number of stars falling into the magnitude range used for a given redshift. We run this test for several limiting magnitudes, and the result for the case of $i = 22.5$ can be seen in Fig. 5.

As already mentioned, the cut in spread model is reliable to an apparent magnitude of 22. Because of that and because of the magnitude dependence of the used colour filters, we do not expect a significant signal up to redshifts of $z \approx 0.5$. This is reflected in Fig. 5, where the signal stays well below 0.01 up to a redshift of 0.55. At a limiting magnitude 22.5, the signal increases to a maximum of 5.2 per cent and for a limiting magnitude of 23 the normalized signal reaches a maximum of 6 per cent. Our cluster follow-up algorithm employs a local background subtraction for redshifts greater than $z = 0.15$. Therefore, a false signal by stars can only be created by a local over density of stars within the investigated aperture of r_{500}.

To explore the impact of star clusters, we perform a second, more extreme test. We identify 29 star clusters in our field and use their locations as an input catalogue for our cluster finder. We use the observed medium luminosity from our RASS sources to define our aperture and radial filter. In 1 out of 29 positions, the filter returns a $\lambda_{\rm MCMF}$ that fulfils our selection criteria to be an optical counterpart of an X-ray source. Two other positions have a $\lambda_{\rm MCMF}$ that exceed three times the Poisson-based measurement error. An investigation of the optical images and galaxy density maps for those three cases reveals two real galaxy clusters next to the position of the star clusters. In fact, two of three star clusters are very close to one another, and thus it is the same galaxy cluster that is found in both cases. Pseudo-colour images showing the star and galaxy clusters are shown in Fig. 6. The redshifts for the clusters are $z = 0.16$ and $z = 0.48$ and therefore below the redshift range where we expect contamination by stars. We note that due to the vicinity to the LMC, a significant fraction of the investigated star clusters consist of young stars associated with the LMC. A repetition of this test with globular clusters is therefore planned once a greater number is observed within the DES.

Finally, we investigate the impact of scattered light caused by bright stars by searching the UCAC4 catalogue (Zacharias et al. 2012) for bright ($V < 11$ mag) sources within 2 arcmin of 2XRS X-ray positions. We investigate the images and galaxy density maps for all 33 cluster candidates that fulfil our standard quality cuts and have a bright source near them. For moderately bright stars we do not observe any effects on the galaxy density contours, indicating that if there are regions affected, these are smaller than the typical smoothing scale. For the brightest sources, the region around the star gets masked due to a lack of identified objects in the photometric catalogue. Thus, the net impact of bright stars is to reduce the area over which optical follow-up of X-ray sources is possible.

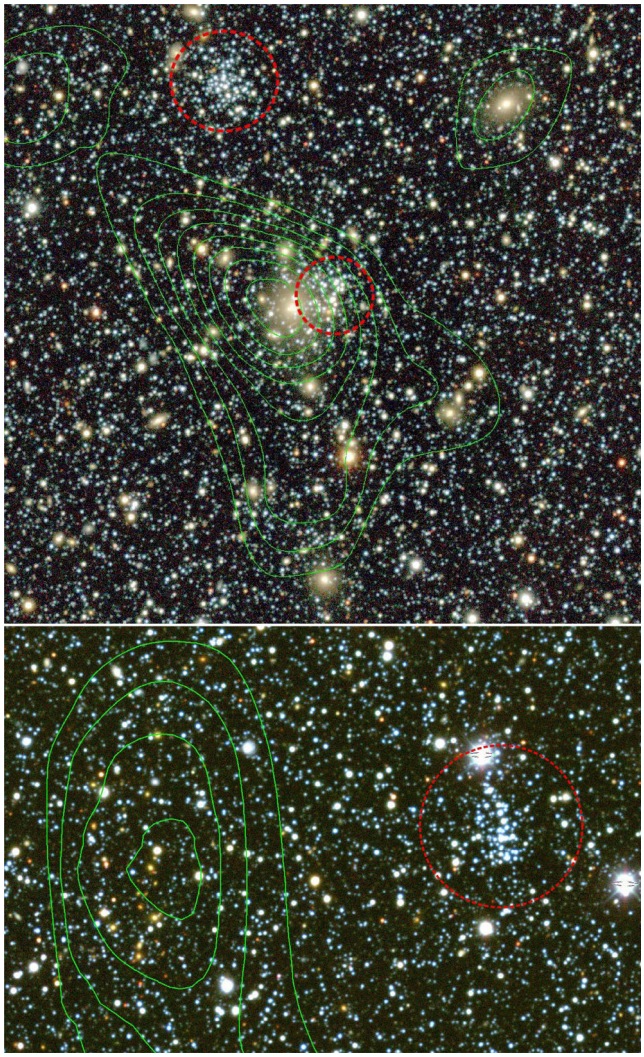

Figure 6. *grz* pseudo-colour images around star cluster positions with significant $\lambda_{\rm MCMF}$ measurements. The image shows the presence of galaxy clusters close to the star cluster positions. The top image shows the case with two star clusters next a galaxy cluster. The galaxy density contours (green) further highlight that the $\lambda_{\rm MCMF}$ peaks found are related to those galaxy clusters and not caused by stars leaking into the galaxy sample. Dashed red circles mark the locations of the star clusters.

4.1.2 X-ray-emitting stars

X-ray-emitting stars tend to be extremely bright in the optical, and therefore, we can use this information to remove any random superpositions of X-ray emitting stars with optical clusters of galaxies. The majority of X-ray emitting stars detected in RASS are too bright to have a valid DES measurement; we therefore cross-match our 2RXS catalogue with the UCAC4 catalogue. In Fig. 7, we show the distribution of UCAC4 sources above 1 arcmin and below

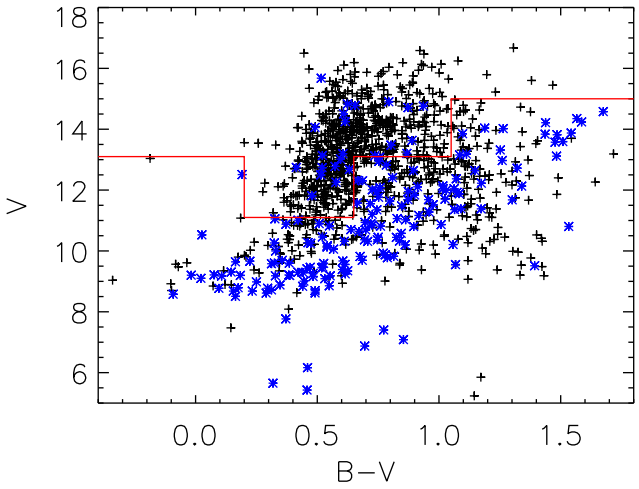

Figure 7. Colour–magnitude distribution of UCAC4 sources within 3 arcmin from the X-ray positions. Sources outside 1 arcmin are plotted as black '+' symbols, sources within 0.5 arcmin are shown as blue '*' symbols. The separation between X-ray and non-X-ray sources is indicated as red line. The radial distribution of both samples can be found in Fig. 8

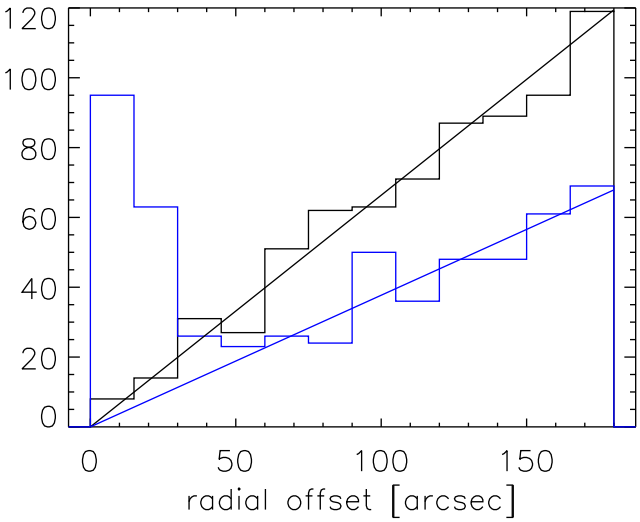

Figure 8. Histogram of separations of UCAC4 sources around 2RXS sources for the two source populations indicated in Fig. 7. Sources with colours and magnitudes falling above the red line of Fig. 7 are used for the black histogram, and sources falling below the red line are shown in the blue histogram. The blue histogram shows a strong excess of sources below 1 arcmin over the expected number of chance superpositions, whose expected distribution is indicated by a blue line. The black histogram is consistent with random superposition, whose expected distribution is shown as a straight line.

0.5 arcmin offset to the X-ray positions. UCAC4 sources with small offsets and therefore high probability of being an optical counter part of the X-ray source seem to cover a distinct region in colour–magnitude space. We split the sources into a non-X-ray emitting and in a potentially X-ray-emitting population based on their position in colour–magnitude space. The distribution of radial offsets to the X-ray position for the two subsamples are shown in Fig. 8. The distribution of non-X-ray emitters in black is consistent with a constant source density, indicated as a black line. The potential X-ray emitters are shown in blue. An excess of sources above the expectation of a constant source density is seen for small offsets within

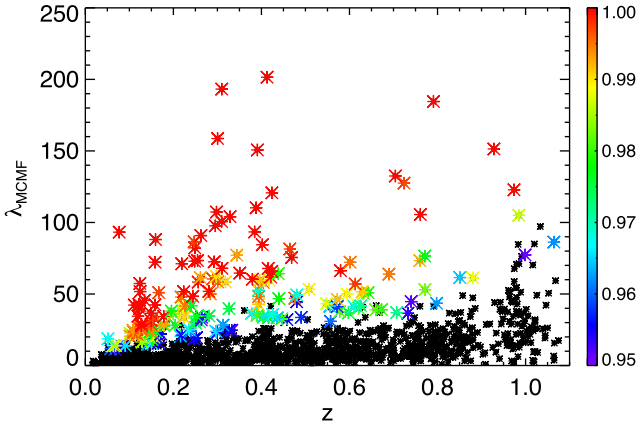

Figure 9. Richness versus redshift distribution for the follow-up sample. Those RASS sources with $P_\lambda < 0.95$, corresponding to more than 5 per cent chance of being a false superposition, are shown in black, and those with $P_\lambda > 0.95$ are colour coded according to P_λ. No cuts on P_s or S are applied.

1 arcmin. We find 160 (153) sources in excess of the background for offsets below 1 arcmin (0.75 arcmin). We use this distribution to assign a probability of a source being an X-ray-emitting UCAC4 source P_* for all sources within 1 arcmin offset to the X-ray position and below the red line in colour–magnitude space. The probabilities are calculated in bins of 15 arcsec and are the ratio of excess counts over total counts. The expected number of chance superpositions is obtained from a fit to the histogram at distances greater 80 arcsec and forcing to be zero at zero distance and is indicated as a blue line in Fig. 8. We find for the first four bins values of 0.970, 0.865, 0.456, and 0.140. Applied to 2RXS catalogue within the DES-SV area, we note that only 4 out of 90 cluster candidates with $P_\lambda > 0.985$ have $P_* > 0.86$. The correlation between bright UCAC4 and 2RXS sources is not included in the creation of the random catalogues. Including those sources would result in a contamination of 3–5 per cent additional to that expected from P_λ alone.

4.2 Galaxy cluster sample

For each 2RXS position, we obtain for up to three peaks the probability that the source is not a random superposition P_λ, the probability of the detection signal-to-noise ratio P_s being greater than null, the signal-to-noise ratio S, the photometric redshift z, the photometric redshift uncertainty σ_z, the richness measurement λ_{MCMF}, the λ_{MCMF} uncertainty σ_λ, and the galaxy density based positions and their offsets from the X-ray position. Additionally, we obtain the X-ray luminosity L_X and the mass M_{500} for each peak using the X-ray count rate, the optically derived redshift and the scaling relations as previously described. Further, we estimate P_* for all 2RXS positions. The distribution of the 1241 RASS sources in λ_{MCMF} and redshift is shown in Fig. 9. Those sources that have $P_\lambda < 0.95$ are shown in black; given their measured richnesses and redshifts, these sources are less than $2\,\sigma$ inconsistent with the distribution of λ_{MCMF} extracted from 1000 random lines of sight. Those above this threshold are colour coded according to their significance in comparison with the random lines of sight.

Depending on the applied cuts in P_λ and P_s, we find up to 100 cluster candidates out of 1241 RASS sources in the DES-SV footprint. The redshifts range from $z = 0.05$ to 0.79. Fig. 10 shows the distribution of RASS sources in redshift for different cuts in P_λ and P_s. Independent of the cut, the cluster with the highest redshift stays in the sample, indicating that this is a robust cluster detection. A

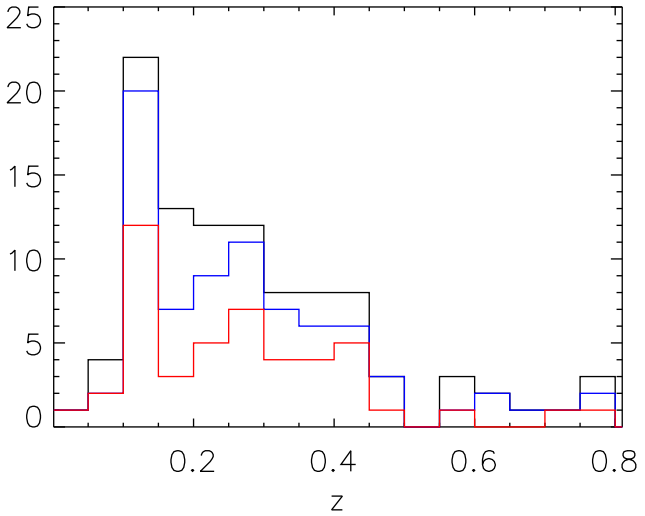

Figure 10. Redshift distribution of RASS clusters with cuts of P_λ and $P_s > 0.98$ in black, P_λ and $P_s > 0.99$ in blue and P_λ and $P_s > 0.999$ in red.

prominent feature in the redshift distribution is visible at redshifts $0.1 < z < 0.15$. This is likely a combination of the lower luminosity (mass) threshold corresponding to the 2XRS flux limit at low redshifts and true large-scale structure, which is also visible in Fig. 1. RASS candidates exceeding P_λ and $P_s > 0.98$ and $P_* < 0.1$ can be found in Table 1.

We find that the cluster candidate list for 2RXS contains some neighbouring sources that share the same optical counterpart. Thus, we carry out an additional filtering step where we examine all 2RXS sources within 5 arcmin of other sources and whose optical counterparts exhibit small differences in redshift $\Delta z < 0.04$. Fourteen cases of multiple 2RXS sources associated with the same cluster are excluded, while two cases that may refer to distinct substructures are kept. Additionally, requiring the centre of the optical counterpart to be within 1.5 arcmin selects 12 of the 14 multiple associations while correctly keeping 2RXS sources associated with distinct substructures. Further testing is needed to finalize the automation of this step, which will be important in studying the 2RXS catalogue over very large solid angle.

As previously noted, the 2RXS catalogue contains only sources that have detection likelihood parameter of at least 6.5, the additional cut of at least six source photons as in 1RXS was dropped. This likelihood or signal-to-noise threshold translates into a position-dependent flux limit, depending on the local exposure time, galactic hydrogen column, and observed background. Given the large variation in exposure times in the region, we study there is a correspondingly large variation in the effective flux limit of the survey. This causes a luminosity-redshift distribution (Fig. 11) without a hard cut at a limiting flux. A flux cut, if preferred, can be applied as a post-processing step.

4.2.1 *Photo-z performance*

To test and calibrate our photometric redshifts, we used two approaches. We first use the same spectroscopic sample as in Section 3.4 to estimate a possible redshift-dependent bias in our photometric redshifts and to measure the scatter of the redshift estimates about the true redshifts. Fig. 12 contains a plot of our photometric redshifts against the spectroscopic redshifts for this sample. To be as close as possible to the measurement method in the DES-SV area, we use the masses listed in Bleem et al. (2015) and

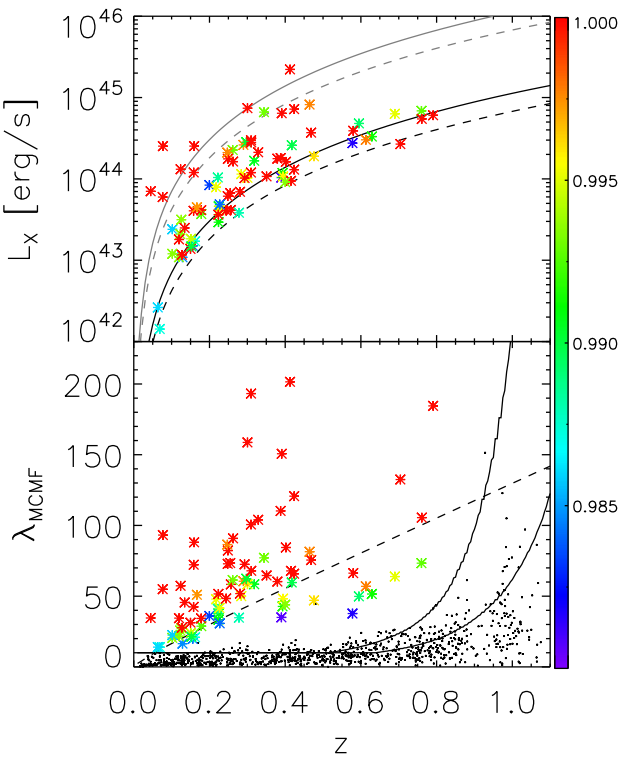

Figure 11. The top panel contains the distribution of RASS+DES-SV clusters in luminosity–redshift space. The thin continuous (dashed) grey lines show the flux limit of REFLEX (REFLEX II). The thick black lines show a flux limit 1/10 of these, indicating that our sample pushes to these flux limits. Below is the distribution of RASS+DES-SV clusters in richness–redshift space. The dashed line indicates 1/10 REFLEX II flux limit converted in λ_{MCMF} using the luminosity λ_{MCMF} relation with $P_{cut} = 0.99$. The solid curves indicate the $S = 3$ limit for $i = 21.5$ mag and $i = 22.1$ mag. Black dots are 2RXS sources with $S < 3$.

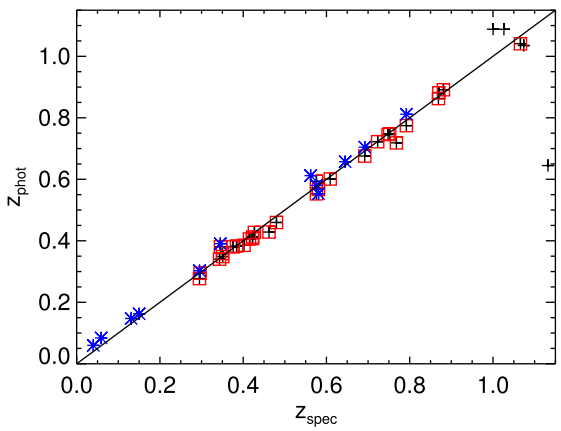

Figure 12. Cluster photometric versus spectroscopic redshifts are plotted (black pluses) for the test sample. Clusters with λ_{MCMF} three times larger than the Poisson uncertainty are marked with red squares, and those in the DES-SV area are marked with blue asterisks.

the luminosity–mass relation to create a virtual count rate, which we then use in our pipeline. Using the SPT-based masses has the advantage of providing a homogeneous mass proxy over that sample. This allows us to probe the photo-z performance of the MCMF beyond the limitation of the depth of the RASS catalogue. We find

and account for a slight redshift-dependent offset between spectroscopic and photometric redshifts of $z_{\rm spec} = z_{\rm phot} \times 0.941 + 0.01$ for this sample of 29 clusters with spectroscopic redshifts. The redshift dependence seen here of 0.941 ± 0.017 might be surprising, given that our RS models are tuned using the same sample. But this redshift dependence can be partially explained due to the fact that the aperture, the used magnitude limit as well as the width of the RS model, change at each step in redshift. The aperture is connected to the assumed luminosity at the given redshift, which increases with redshift. Similarly, the allowed magnitude and colour range of the sources considered in our matched filter increases with redshift due to the evolution on $m*$ and measurement errors. All this can lead to the inclusion of faint cluster sources that were fainter or have colours that were slightly off from the RS model. All these effects cause a tendency for $\lambda_{\rm MCMF}$ to peak at a redshift that is slightly higher than the redshift of the cluster, even though the RS model is correct at the true cluster redshift.

We apply this correction and probe richnesses up to a redshift of $z = 1.1$, expecting to get reliable redshifts out to $z \approx 1$. The latter restriction comes from the difficulty to find and fit a peak if there are not enough points probing the drop in $\lambda_{\rm MCMF}$ expected at redshifts beyond that of the cluster. Using this sample of 29 clusters with $S > 3$, we obtain a characteristic scatter $\sigma_{\Delta z/(1+z)} = 0.010$, using an outlier resistant standard deviation.[1] We note from our data that $S > 2.5$ appears to be sufficient to obtain good photo-z estimates, but at this lower signal-to-noise ratio, it appears there are also outliers at redshifts $z > 1$.

We also check whether known clusters in the SPT-East field give similar performance. We search the MCXC (Piffaretti et al. 2011), the BAX (Sadat et al. 2004), and the Abell (Abell 1958) catalogues and match the positions with our RASS catalogue, using the position and count rate from 2RXS as input. All told, we find 12 clusters that have signal-to-noise ratio $S > 2.5$. For those clusters we find a characteristic scatter of $\sigma_{\Delta z/(1+z)} = 0.014$. We find no evidence for a bias in the cluster photometric redshifts in the overlapping redshift range.

4.2.2 *Scaling relations*

We use the scaling relation between $\lambda_{\rm MCMF}$ and luminosity or mass as a tool to understand selection effects and to test the basic properties of the sample. Contamination of the cluster sample by non-clusters will affect intrinsic scatter and other basic scaling relation parameters. With increasing cut in P_λ and with the corresponding increasing in sample purity, we expect the intrinsic scatter to fall and scaling relation parameters to stabilize once a clean sample is obtained.

A well-behaved scaling between $\lambda_{\rm MCMF}$ and mass proxies can be expected by construction of our richness estimator. However, this is not crucial for the success of our confirmation process, since P_λ the main parameter for confirmation completely works self-consistent in $\lambda_{\rm MCMF}$ space. This makes P_λ more robust against changes in the scaling relations such as redshift evolution, which would affect all $\lambda_{\rm MCMF}$ in the same way, leaving P_λ unchanged. Due to its design as a conformation tool, there will always be other mass proxies available that are based on the method the original catalogue is drawn from. Such proxies, like the X-ray luminosity in this work, will be considered as the main mass proxy for future analysis. The richness $\lambda_{\rm MCMF}$ might be used as a secondary mass proxy if correlations are taken into account.

We stress here that the luminosities given here are based on a simplistic model with a fixed temperature and the X-ray fluxes typically within a fixed aperture of 5 arcmin diameter. Masses are derived from these luminosities using the Mantz et al. (2010b) scaling relation assuming that the measured flux corresponds to a measurement within r_{500}. Masses of the SPT cluster sample are taken from Bleem et al. (2015), while the $\lambda_{\rm MCMF}$ is derived using a mock X-ray count rate as input. This count rate is derived from the mass, using the spectroscopic redshift and the mass–luminosity scaling relation with fixed temperature. These assumptions have to be taken into account when comparing to other publications, but in general these have only a small impact on MCMF performance.

We use here the assumption that the scaling relations follow a simple power law of the form

$$\left\langle \lambda'_{\rm MCMF}(x) \right\rangle = A x^B, \tag{12}$$

where $\lambda'_{\rm MCMF}$ is the scaled richness, A is the normalization, B is the power-law index and x is either the scaled luminosity or mass. For the pivot of the scaling relations, we choose 10^{44} erg s^{-1} for the luminosity and $4 \times 10^{14}\,{\rm M}_\odot$ for the mass-based scaling relation. We scale our richness by dividing $\lambda_{\rm MCMF}$ by 90.

We fit our scaling relation model to the data using a maximum-likelihood method described in Kelly (2007) to find the best-fitting power law to our data, including lognormal intrinsic scatter, accounting for measurement errors in the x- and y-direction and the Malmquist bias. We used the implementation described in Sommer & Basu (2014) that directly fits a power law to the data instead of transferring the problem to log–log space to use the original implementation given in Kelly (2007). The individual fit results for different selection cuts are listed in Table 2. Intrinsic scatter is given in log-space using the natural logarithm.

Fig. 13 contains a plot of the $\lambda_{\rm MCMF}$ and X-ray luminosity distribution of the sample, where we have included not only the colour-coded systems with high probability of being real $P_\lambda > 0.95$ but also (in black) those systems that include contamination from false superpositions. There is no clear separation in the distribution, although there are many systems piled up in the low-significance black points. This indicates that the scaling relation parameters will be sensitive to the significance cuts applied to the data.

Fig. 14 is a plot of the dependence of the best-fitting scaling relation parameters on the selection parameter $P_{\rm cut}$, which is the minimum value in either P_λ or $P_{\rm s}$ that is applied in the sample selection. There is a suggestion that the intrinsic scatter shrinks with increasing $P_{\rm cut}$, which is increasing sample purity. For the $\lambda_{\rm MCMF}$–mass relation, the intrinsic scatter becomes constant at $P_{\rm cut} = 0.985$. For the $\lambda_{\rm MCMF}$–luminosity relation, the intrinsic scatter is constantly decreasing with increasing $P_{\rm cut}$, although the trend may not be significant for cut values above 0.985. But broadly speaking, this analysis suggests that with sufficiently high $P_{\rm cut}$ values one obtains a sample that exhibits scaling relations that are insensitive to the exact value of the cut.

While the slopes of the scaling relations seem to be robust against the chosen $P_{\rm cut}$, there is a somewhat different behaviour exhibited by the SPT and RASS-based $\lambda_{\rm MCMF}$–mass relations. Fig. 15 shows these samples plotted, providing some insights into the slope differences. Overall, the RASS sample seems to be a reasonable extension of the SPT sample towards lower masses.

[1] We use the IDL function robust_sigma.pro from the IDL Astronomy Users Library (http://www.idlastro.gsfc.nasa.gov).

Table 2. Dependence of scaling relation parameters on the lower limit $P_{\rm cut}$ applied to P_λ and $P_{\rm s}$, for the $\lambda_{\rm MCMF}$–luminosity relation (L), $\lambda_{\rm MCMF}$–mass relation (M) of 2RXS sources and for the $\lambda_{\rm MCMF}$–mass relation for SPT clusters with spectroscopic redshifts (S). $S_{\rm min}$ lists the lowest value of S in that sample, N is the number of cluster candidates and Cont. the expected contamination by random superpositions based on equation (13).

	$\lambda_{\rm MCMF}$–luminosity						$\lambda_{\rm MCMF}$–mass 2RXS						$\lambda_{\rm MCMF}$–mass SPT								
$P_{\rm cut}$	$A_{\rm L}$	$eA_{\rm L}$	$B_{\rm L}$	$eB_{\rm L}$	$\sigma_{\rm int,L}$	$e\sigma_{\rm int,L}$	$A_{\rm M}$	$eA_{\rm M}$	$B_{\rm M}$	$eB_{\rm M}$	$\sigma_{\rm int,M}$	$e\sigma_{\rm int,M}$	$A_{\rm S}$	$eA_{\rm S}$	$B_{\rm S}$	$eB_{\rm S}$	$\sigma_{\rm int,S}$	$e\sigma_{\rm int,S}$	$S_{\rm min}$	N	Cont.%
0.950	0.50	0.02	0.34	0.03	0.40	0.03	0.72	0.03	0.51	0.03	0.32	0.02	0.86	0.08	0.93	0.13	0.30	0.06	3.5	134	43
0.955	0.51	0.02	0.32	0.02	0.39	0.03	0.75	0.04	0.55	0.04	0.36	0.03	0.87	0.08	1.10	0.14	0.27	0.05	3.5	128	41
0.960	0.52	0.02	0.33	0.03	0.37	0.02	0.76	0.04	0.52	0.04	0.36	0.03	0.80	0.06	1.13	0.12	0.25	0.06	3.5	121	39
0.965	0.54	0.02	0.33	0.03	0.38	0.03	0.76	0.04	0.49	0.04	0.34	0.03	0.88	0.07	1.02	0.12	0.28	0.04	3.5	113	36
0.970	0.59	0.02	0.32	0.02	0.34	0.03	0.82	0.04	0.56	0.04	0.33	0.03	0.81	0.05	1.16	0.11	0.22	0.05	3.5	101	35
0.975	0.57	0.02	0.36	0.03	0.35	0.03	0.85	0.04	0.54	0.04	0.31	0.02	0.79	0.05	1.19	0.11	0.22	0.05	3.5	98	30
0.980	0.62	0.02	0.38	0.03	0.28	0.03	0.93	0.05	0.57	0.05	0.27	0.03	0.85	0.09	1.08	0.15	0.29	0.06	3.5	88	27
0.985	0.65	0.02	0.38	0.03	0.25	0.02	0.94	0.04	0.56	0.04	0.25	0.04	0.96	0.08	0.95	0.12	0.24	0.06	3.7	78	23
0.990	0.66	0.02	0.44	0.02	0.20	0.02	1.00	0.04	0.58	0.05	0.23	0.03	0.92	0.07	0.99	0.12	0.21	0.04	4.2	66	18
0.995	0.72	0.03	0.37	0.03	0.23	0.03	1.02	0.05	0.57	0.05	0.25	0.03	0.89	0.06	1.09	0.10	0.19	0.03	4.5	54	11
0.999	0.75	0.03	0.40	0.03	0.21	0.03	1.12	0.06	0.63	0.07	0.25	0.04	0.94	0.09	0.88	0.14	0.26	0.05	5.3	39	3

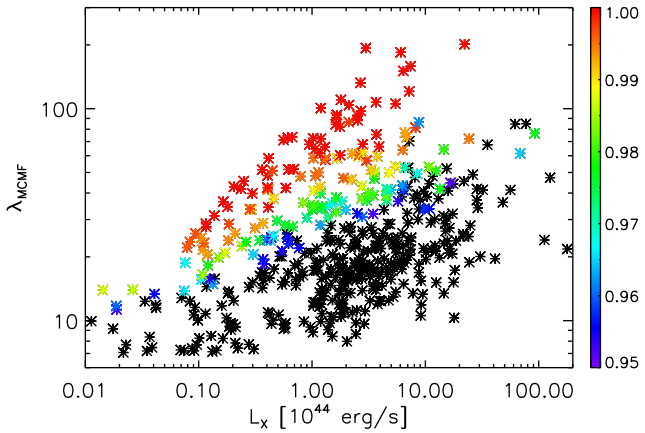

Figure 13. Richness versus luminosity. All RASS sources with $\lambda_{\rm MCMF}$ based detection probability P_λ <0.95 and statistical signal to noise ratio $S < 2.5$ are shown in black. Those sources with $P_\lambda > 0.95$ and $S > 2.5$ are colour coded according to P_λ.

4.2.3 Cluster catalogue contamination

With the information from MCMF, it is straightforward to characterize the contamination due to chance superposition of a non-cluster X-ray source with an optical cluster counterpart. As described in Section 3.8, we use follow-up of a large catalogue of random positions to characterize the probability P_λ of obtaining a particular richness $\lambda_{\rm MCMF}$ as a function of redshift for our sample. The process of following up a candidate catalogue and imposing a threshold value $P_{\rm cut}$ in P_λ of $P_{\rm cut} = 0.97$, for example, then implies that 3 per cent of the candidate sources that are not clusters will be matched to what are in actuality random superpositions. Thus, the final contamination fraction $f_{\rm c}$ of the resulting MCMF cluster catalogue depends on the threshold $P_{\rm cut}$ and the contamination in the original candidate catalogue:

$$f_{\rm c} = \frac{N_{\rm cont}}{N_{\rm cat}} = \frac{(1-P_{\rm cut})}{P_{\rm cut}} \frac{(N_{\rm cand}-N_{\rm cat})}{N_{\rm cat}}, \qquad (13)$$

where the input candidate catalogue contains $N_{\rm cand}$ members of which $N_{\rm cont}$ are non-cluster, and the final cluster catalogue has $N_{\rm cat}$ members (including any contamination that has slipped through).

The 2RXS candidate catalogue is highly contaminated, with only a small fraction of sources corresponding to real clusters. Approximately 22 per cent of the sources are spurious, and roughly 90 per cent of the real sources are either active galactic nucleus (AGN) or stars. Nevertheless, with an appropriate threshold in P_λ it is possible to produce cluster catalogues with very low contamination. As an example, if we adopt $P_{\rm cut} > 0.999$ applied to the 1241 2RXS sources overlapping DES-SV, we find 39 clusters. Given these numbers, equation (13) indicated that we would expect a contamination fraction $f_{\rm c} = 3$ per cent or that ∼1.2 of those 39 clusters in the output catalogue are random superpositions. In Table 2, we list the expected contamination for the different selections used to investigate the dependence of the scaling relation on those cuts.

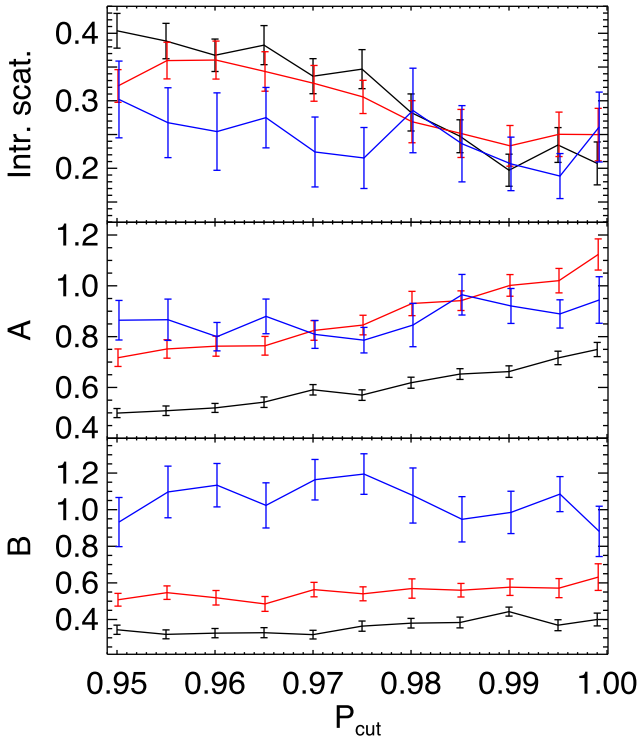

Figure 14. Intrinsic scatter, normalization (A) and power-law index (B) of the L–$\lambda'_{\rm MCMF}$ (black) and M–$\lambda'_{\rm MCMF}$ (red) scaling relation of RASS cluster candidates and M–$\lambda'_{\rm MCMF}$ scaling relation of SPT clusters (blue) against cut in P_λ and $P_{\rm s}$. In the case of SPT, we adopt a lower cut in S corresponding to the minimum S found for RASS clusters at this cut in P_λ and $P_{\rm s}$.

For eROSITA we expect the situation to be much better, indeed. The PSF size for the eROSITA survey is expected to be

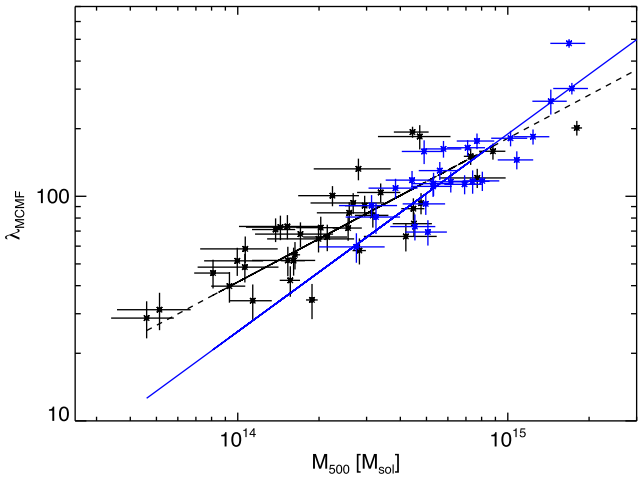

Figure 15. Richness–mass relation: Distribution of 2RXS sources with P_λ and $P_s > 0.999$ are shown in black, SPT clusters from the spectroscopic sample are shown in blue. Best-fitting scaling relations for the corresponding cut are shown as black dashed and blue continuous lines.

∼25 arcsec half-energy width, which is comparable to the PSF within the inner ring of *ROSAT* PSPC pointed observations. Vikhlinin et al. (1998) used the extent of X-ray sources in his serendipitous survey to identify clusters, demonstrating a contamination of between ∼2 and 10 per cent (depending on the flux limit) in a sample of somewhat more than 200 clusters. The application of MCMF to a input candidate catalogue with 10 per cent contamination would result in a final cluster catalogue contamination fraction that is one to two orders of magnitude below the contaminations listed in Table 2.

4.2.4 Centering

For each cluster candidate, we estimate a centre based on the galaxy density maps of RS galaxies at the cluster redshift. The maps are created using Voronoi Tessellation and smoothed with a 250 kpc kernel. The centre position is the average between the position of the nearest density peak and the barycenter of the same peak, found by `SExtractor`.

The positional accuracy for point sources is measured for the RASS to be of 0.3 arcmin (Voges et al. 2000). Despite the fact that most of the RASS clusters appear to be point like due to the large survey PSF of the RASS, the true surface brightness distribution is extended and can be of complex shape. Fig. 16 shows the distribution of offsets between galaxy-based and X-ray-based centres for the RASS cluster sample as well as the offset distribution between SZE (Sunyaev & Zel'dovich 1970) based and galaxy density based centres for the SPT cluster sample. The distribution of RASS centre offsets is significantly broader than that of the SPT sample or that expected for RASS point sources.

4.3 Comparison to other cluster catalogues

The DES-SV field used for this work is overlapped by the SPT survey area and the MCXC cluster catalogue. Moreover, these DES-SV data have been used to construct a RedMaPPer cluster catalogue. In this section, we compare our RASS+DES-SV catalogue to these other catalogues.

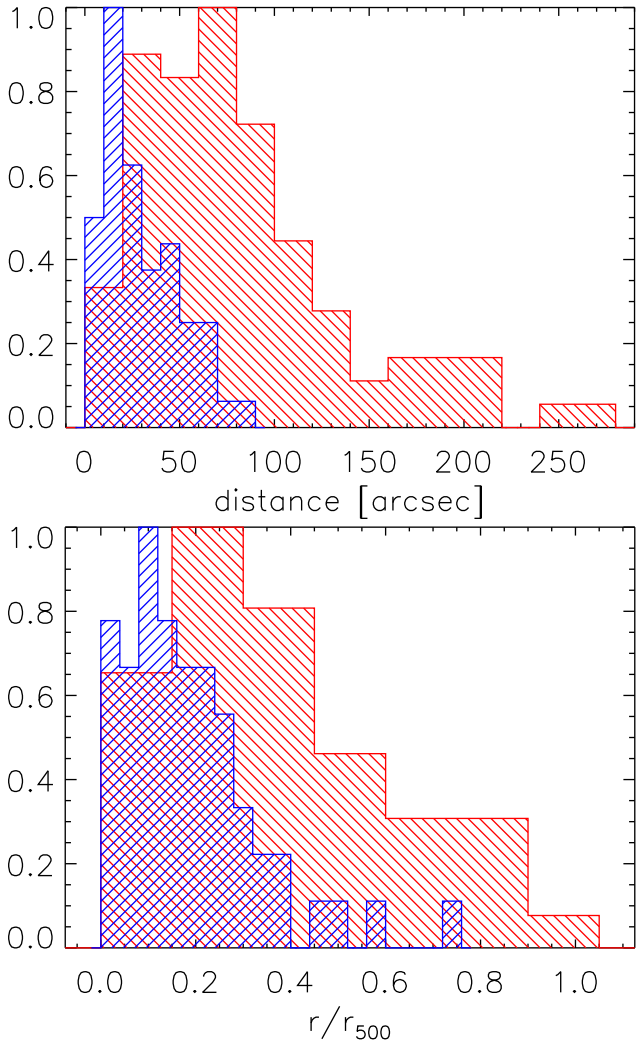

Figure 16. Distribution of offsets between X-ray and galaxy density centre (red) for the $P_{cut} > 0.98$ sample and between galaxy density centre and SPT centre (blue) for the SPT cluster sample. The peak of the distributions are normalized to one.

4.3.1 SPT-SZ clusters

We find 56 SZE-selected clusters from SPT in the investigated area, and 22 of these clusters have an RASS detection within 4 arcmin. These numbers will significantly increase once we extend our analysis to the full 2500 deg^2 SPT-SZ survey region. Eight clusters fall below our selection criteria of $P_\lambda > 0.98$ and $P_s > 0.98$, but only four have $P_\lambda < 0.97$. All four of these SPT clusters have redshifts $z > 0.55$ and all except one have offsets from the corresponding 2RXS source larger than 2 arcmin. Of these four systems, all but one is well detected in our optical cluster finder, but the λ_{MCMF} falls in a range where there is a greater than 3 per cent chance of a random superposition. The second lowest significance cluster out of these four clusters has an X-ray to SZE centre offset of 1.3 arcmin, an SZE-based mass estimate of $M_{500} = 3.76 \times 10^{14}$ M$_\odot$ and a photo-z estimate of $z = 0.76 \pm 0.03$. Our results for this cluster include a photo-z estimate of $z = 0.706$ and an X-ray-based mass of $M_{500} = 4.0 \times 10^{14}$ M$_\odot$. Thus, we find consistent cluster parameters, although this falls near the lower limit for optical confirmation at that redshift.

Only one cluster match, SPT-CLJ0432-6150, falls significantly below the standard selection criteria and shows a small X-ray to SZE positional offset of 0.5 arcmin. The signal-to-noise ratio of the optical counterpart is $S = 2.4$, and it exhibits significances of $P_\lambda = 0.64$ and $P_s = 0.65$ at a redshift of $z = 0.63$. The SPT-based mass estimate is $M_{500} = (2.39 \pm 0.65) \times 10^{14}\,M_\odot$, and the photometric redshift is given as $z = 0.98 \pm 0.07$. Using the RASS X-ray count rate and the redshift from SPT, we obtain an X-ray-based mass of $M_{500} = 3.5 \times 10^{14}\,M_\odot$, which is consistent with the SZE-based mass estimate. Based on the flux limit, we see in Fig. 11 and using the Mantz et al. (2010b) scaling relation we expect a mass limit at $z = 0.98$ of about $M_{500} = 5.2 \times 10^{14}\,M_\odot$, which is clearly above the mass estimates from X-ray and SZE. So given the low significances of the $z = 0.63$ counterpart, if we had sufficiently deep optical data at this location, we would have likely identified the higher redshift counterpart and rejected the counterpart at $z = 0.63$.

To further clarify whether the cluster is a misidentified lower redshift cluster or a missed high-z cluster, we utilize the galaxy density map automatically created for each peak in λ_{MCMF} and overlaid on the *grz* pseudo-colour image. Because the photometric redshift suggested in Bleem et al. (2015) would place the optical counterpart near our adopted depth limits, we relax our standard depth setting, effectively changing our magnitude limit from $i = 21.8$ to $i = 22.1$.

The λ_{MCMF} versus redshift plot using this high-z extension can be seen in Fig. 17. As one can see, the modified settings do indeed show a cluster candidate at a redshift of $z \sim 1.09$ and a λ_{MCMF} of 86 ± 40. For this redshift, we obtain an X-ray-based mass of $5.1 \times 10^{14}\,M_\odot$, which is nearer to the flux-limit-induced mass of $5.7 \times 10^{14}\,M_\odot$. However, the λ_{MCMF} supports a lower mass estimate of $3.2 \times 10^{14}\,M_\odot$, closer to the SZE-based mass estimate. The galaxy density contours of the peak at $z = 1.09$ are in agreement with the X-ray and SZE positions, supporting the high-redshift cluster and disfavouring the $z = 0.63$ structure. The differences between X-ray-, SZE-, and λ_{MCMF}-based masses suggest that the X-ray flux is likely boosted by other sources, such as AGN or the observed structure at $z = 0.63$. Our photometric redshift seems to be consistent with that presented in Bleem et al. (2015) within 2σ, while suggesting a slightly higher redshift for that cluster. This example illustrates the importance of having a strong positional prior (and to a lesser extent mass prior) when identifying optical counterparts of X-ray- or SZE-selected clusters.

As a further consistency check, we search for the highest mass RASS clusters missing in the SPT cluster sample. The cluster with the highest X-ray mass that does not have an SPT counterpart is at $z = 0.76$ and has a mass of $M_{500} = 4.6 \times 10^{14}\,M_\odot$ and a λ_{MCMF}-based mass estimate of $M_{500} = 4.1 \times 10^{14}\,M_\odot$. This makes it also the second richest cluster that is missing. The richest cluster missing has a λ_{MCMF} of 136, corresponding to mass of $M_{500} = 5.8 \times 10^{14}\,M_\odot$ using our best-fitting scaling relation. The X-ray-based mass estimate is $M_{500} = 2.75 \times 10^{14}\,M_\odot$, suggesting a significantly lower mass. Judging from fig. 7 of Bleem et al. (2015), the cluster masses are in the range where the SPT cluster sample is only ~50 per cent complete. Finding a missing cluster is therefore not in contradiction with the expectations. The larger sample enabled by the extension of this work to the full survey will enable a detailed quantitative consistency test of the sample as applied in Saro et al. (2015).

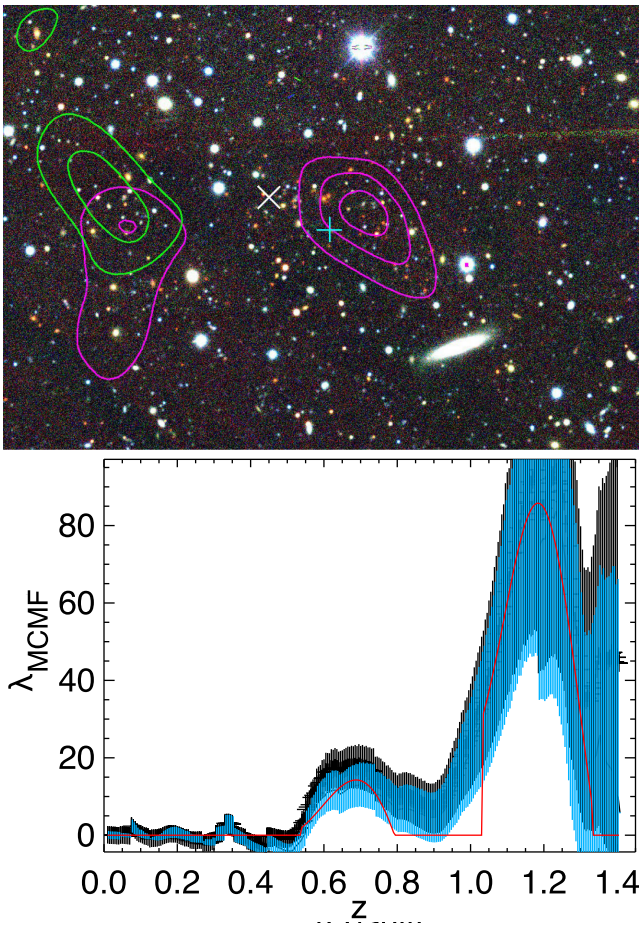

Figure 17. Top panel: *g*, *r*, *z* pseudo-colour image of the central 5×3.5 arcmin region around the RASS detection close to cluster SPT-CLJ0432-6150, not identified with our standard settings. Cyan cross: RASS position; white cross: SPT position; green contours: galaxy density for $z = 0.63$ galaxies; magenta contours: galaxy density for $z = 1.09$ galaxies. Lower panel: richness versus redshift plot, with modifications to explore higher redshifts.

4.3.2 *MCXC clusters*

The MCXC (Piffaretti et al. 2011) catalogue is a meta-catalogue of X-ray-detected clusters of galaxies and combines various publicly available RASS-based X-ray catalogues, such as NORAS (Böhringer et al. 2000), REFLEX(Böhringer et al. 2004), and MACS (Ebeling, Edge & Henry 2001). We find seven matches between 2RXS and MCXC in our footprint, using a cross-identification radius of 3 arcmin. The largest offset between 2RXS and MCXC matches is 1.5 arcmin and the mean offset is 0.75 arcmin. We find for all except one of these matches significance values of $S > 3$, $P_\lambda > 0.78$, and $P_s > 0.86$.

The only match with $S < 3$ has significance values of $S = 1.7$, $P_\lambda = 0.35$ and $P_s = 0.32$. This is well below the threshold required to rule out a chance superposition or to consider it even a statistically significant detection. The MCXC catalogue lists a mass of $M_{500} = 7 \times 10^{13}\,M_\odot$ and a redshift of $z = 0.33$. A cluster of that mass would have been detected at that location with $S > 5$. Optical investigation at the MCXC location does not show an obvious cluster counterpart. No additional X-ray data besides those from *ROSAT* were found for that location. This cluster was originally published in the southern SHARC catalogue (Burke et al. 2003), and is the only one in that catalogue with a quality flag of three. We therefore conclude that this MCXC cluster is not a real cluster.

4.3.3 RedMaPPer clusters

A natural source for comparison is the RedMaPPer catalogue for the same region (Rykoff et al. 2016). Although there are similarities between MCMF and RedMaPPer in the radial and colour filter, there are a few things that may cause differences in the output catalogues. First, RedMaPPer is a cluster finder, while our code is tuned for cluster confirmation around X-ray positions. Also, in MCMF there is no recentering to the optical counterpart position. Our aperture for counting galaxies is defined by the mass implied by the X-ray luminosity. Further, we use independently derived RS models and data reduction pipelines. In the remainder of the section, we focus, in turn, on (1) high significance 2RXS clusters from our catalogue that are missing in the RedMaPPer catalogue, (2) high $\lambda_{\rm RM}$ RedMaPPer systems missing in our catalogue, and then (3) 2RXS clusters from our catalogue with RedMaPPer catalogue counterparts.

First, we search for 2RXS cluster candidates with $P_\lambda > 0.99$ (there are 60 of these) that have no RedMaPPer cluster candidate within a distance of 2.5 arcmin. We find 14 such clusters, 4 of which lie outside the footprint of the RedMaPPer cluster catalogue. In three cases, the 2RXS position has a offset of >150 arcsec from the main galaxy density peak, which itself is consistent with a RedMaPPer cluster. In one case, the BCG was not correctly identified by RedMaPPer. Three clusters fall close to stars, where different masking strategies may have led to the non-detections in the RedMaPPer catalogue. One cluster, 2RXC J0426.5-6003 ($z = 0.06$), falls below the lower redshift limit of $z = 0.1$, applied to the RedMaPPer catalogue. The neighbouring cluster 2RXC J0428.4-5349 at $z = 0.26$ is not in the RedMaPPer catalogue either. Both clusters are part of the region with three distinct redshift peaks shown in Fig. 4 and might have been excluded by RedMaPPer due to masking of bright cluster members in the low-z clusters. The last missing cluster 2RXC J0536.2-5847 was excluded from the RedMapper catalogue because a large fraction of the cluster region was masked. We note that in our data set the cluster region does not suffer from significant masking.

Secondly, we search for RedMaPPer clusters with $\lambda_{\rm RM} > 60$ that do not have a 2RXS cluster candidate having $P_\lambda > 0.99$ within 4 arcsec. This is motivated by the observed offset distribution in Fig. 16 and the limits seen in Fig. 11. We find 19 RedMaPPer clusters with a median redshift of $z = 0.59$. This high median redshift already suggests that those system may be too high in redshift and to low in mass to be detected in 2RXS. The cluster with the highest richness missed by 2RXS has $\lambda_{\rm RM} = 107$, a redshift $z_{\rm RM} = 0.76$ and is the fifth highest redshift cluster without a 2RXS counterpart. A cluster of this richness and redshift is close to the detection limit of 2RXS, as can be seen in Fig. 11. This is true even given the small systematic offset between $\lambda_{\rm RM}$ and $\lambda_{\rm MCMF}$ discussed in the following paragraph and given the intrinsic scatter between luminosity and richness. The same arguments hold for all clusters down to redshift 0.4, noting that the second richest missing cluster has only a richness of $\lambda_{\rm RM} = 87$ at $z_{\rm RM} = 0.81$. Concentrating on the low redshift range, we find five missing clusters with $0.26 < z_{\rm RM} < 0.43$ with a range in richness of $60 < \lambda_{\rm RM} < 77$. Three of them are in regions with RASS exposure times below half of the median exposure time. Another cluster lies in a region with 80 per cent of the median exposure time. The remaining cluster that is not in a particularly low exposure time region has $\lambda_{\rm RM} = 75$ and $z_{\rm RM} = 0.316$. The nearest 2RXS source is 2RXC J0434.6-4726 that is 6 arcmin away from the RedMaPPer position and is shown in Fig. 18. MCMF identifies this 2RXS candidate as a cluster with redshift of $z_{\rm MCMF} = 0.310$ and richness $\lambda_{\rm MCMF} = 68$ but assigns the optical centre to a local over density of galaxies likely associated with the main cluster.

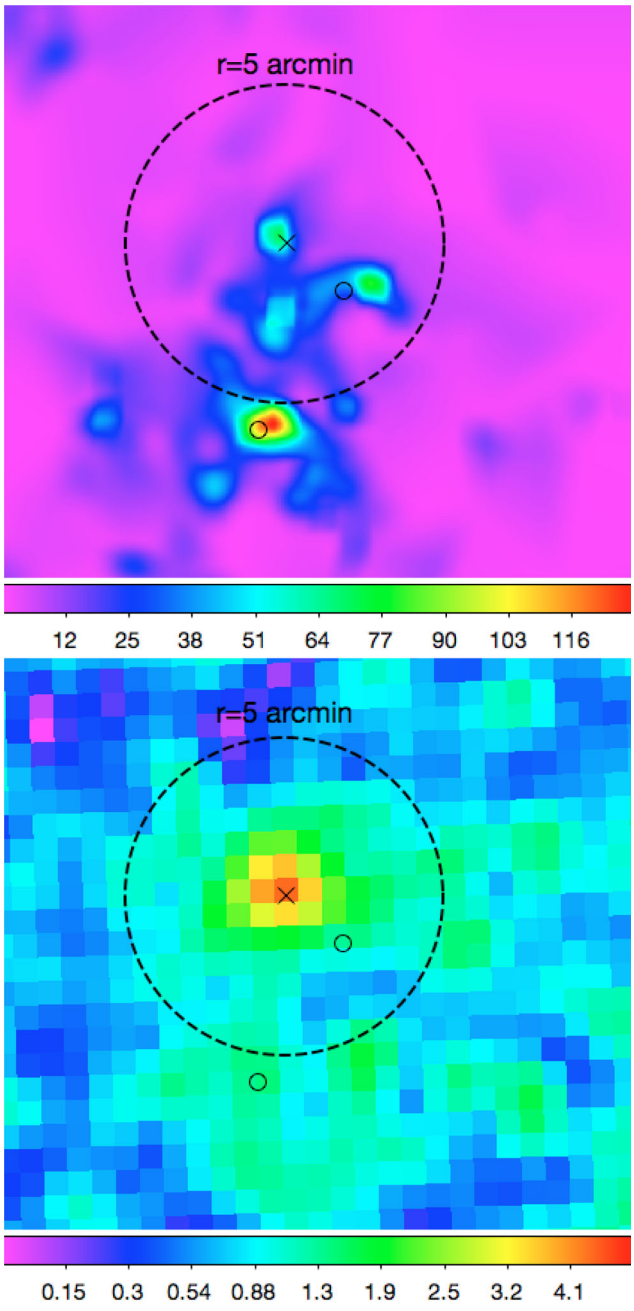

Figure 18. Region around 2RXC J0434.6-4726. Top: galaxy density map of RS galaxies at $z = 0.31$. Bottom: smoothed RASS photon count image in the energy range of 0.1−2.4 keV of the same region. The black cross marks the 2RXS position, the dashed circle marks the extraction region of the 2RXS measurement of 5 arcmin, corresponding to 1.4 Mpc at $z = 0.31$. The small black circle close to the main galaxy density peak marks the position of the RedMaPPer cluster of $\lambda_{\rm RM} = 75$ and $z_{\rm RM} = 0.316$ discussed in Section 4.3.3. The small black circle within 5 arcmin from the 2RXS source corresponds to a RedMaPPer cluster of $\lambda_{\rm RM} = 11$ and $z_{\rm RM} = 0.29$.

In the current incarnation, MCMF simply searches for the nearest peak in the RS-weighted galaxy density map. It does not perform any likelihood analysis to identify the most likely galaxy density peak associated with the cluster candidate given richness or luminosity. Otherwise, the code would have shown a large X-ray to optical offset, which would have indicated a likely correlated X-ray point source. In total, we do not see strong evidence for missing

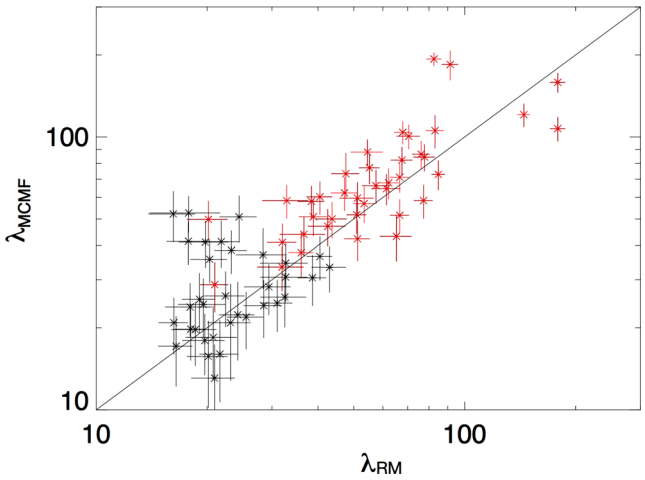

Figure 19. Richness comparison for matches between the RASS+DES-SV and RedMaPPer catalogues. Highlighted in red are clusters with $\lambda > 20$ and $P_{\rm cut} > 0.98$. The black line shows $\lambda_{\rm MCMF} = \lambda_{\rm RM}$.

RedMaPPer clusters in 2RXS that should have been detected, but the large offset of 2RXC J0434.6-4726 is a failure mode that underscores the current limitations of MCMF.

Finally, we match the catalogues by searching for the nearest RedMaPPer counterpart that lies within 2.5 arcmin of each of our clusters. Requiring $\lambda_{\rm RM} > 15$ and $S > 2.5$, we find 73 matches. Restricting the catalogue to $\lambda_{\rm RM} > 20$ as suggested by Rykoff et al. (2016), we find 60 matches. Note that the RedMaPPer catalogue only exists for $\delta > -61^\circ$. The corresponding redshift scatter is $\sigma_{\Delta z/(1+z)} = 0.011$ for both of these catalogues. Given that the same raw data are used in both cases, this scatter reflects the differences in the algorithms, indicating that there is good agreement between the two codes.

Fig. 19 contains a comparison of the richnesses we measure $\lambda_{\rm MCMF}$ versus the RedMaPPer richnesses $\lambda_{\rm RM}$. Although we developed our code to enable a precise and quantitative selection of the optical counterpart with different radial and colour weighting than the RedMaPPer algorithm, the $\lambda_{\rm MCMF}$'s we measure are clearly well correlated to $\lambda_{\rm RM}$. The upcoming larger RASS-selected sample from the full DES data set will enable a more extensive comparison.

Considering all matches with $\lambda_{\rm RM} > 20$ and $|z_{\rm MCMF} - z_{\rm RM}|/(1 + z_{\rm RM}) < 0.04$, we find a median offset between RedMaPPer and 2RXS positions of 1.65 arcmin. For the same sample, we find an offset between our optical centres to RedMaPPer centres of about 0.33 arcmin and between our centres and 2RXS of 1.15 arcmin. If we restrict the comparison to the P_λ and $P_{\rm s} > 0.98$ sample, we find 41 matches. Here, the median offset between RedMaPPer and 2RXS reduces to 1.1 arcmin and is only marginally larger than the median offset between 2RXS and our centres of 1 arcmin. The median offset between RedMaPPer and our centres stay at 0.33 arcmin for this sub-sample. The lower average offset of our centres to 2RXS can be explained by two effects. First our method simply searches for peaks towards the 2RXS sources, while the RedMaPPer centres are found independently. A second argument is the potential problem of the RedMaPPer algorithm to find the BCG candidate for very low redshift systems where saturation and blending effects may play an important role. Our algorithm uses smoothed density maps, which allows us to recover the correct cluster centre even when the brightest cluster members are saturated or blended.

In summary, we see very good agreement between the characteristics of the matched sample of RedMaPPer clusters and our own, three examples of 2RXS systems not making it into the RedMaPPer catalogue, and a case of a 2RXS system that could be an X-ray point source that has been associated with a clump of RS galaxies that lie in the outskirts of a larger optical system identified by RedMaPPer. The analysis of the 2RXS cluster sample extracted from the full DES region will allow more precise cross-checks with RedMaPPer.

5 CONCLUSIONS

In this work, we present our multicomponent matched filter cluster confirmation method MCMF and apply it to the 2RXS X-ray source catalogue (Boller et al. 2016), using the DES-SV optical data set. We identify optical counterparts using the overdensity of galaxies having colours consistent with the RS, extracting richnesses $\lambda_{\rm MCMF}$ and photometric redshifts, and then quantifying the probability that the identified counterpart is a random superposition of an unassociated optical system. We present a catalogue of 88 RASS selected, MCMF confirmed clusters that cover a redshift range from $0.05 < z < 0.8$ and a mass range of 2×10^{13} to $2 \times 10^{15}\,{\rm M}_\odot$. With our MCMF method, we follow up sources that are as much as 10 times fainter than the typical sources previously used to identify RASS galaxy cluster samples. When restricting to more conservative cuts of $P_{\rm cut} > 0.999$, we find 39 clusters with an expected contamination of 3 per cent, which is about 10 times the number of identified REFLEX clusters within the same footprint. The contamination of the cluster catalogue by random superpositions can be directly derived from the catalogue, given the adopted $P_{\rm cut}$, which enables one to use MCMF to create cluster catalogues with the desired contamination.

In addition to following up RASS-selected sources, we follow up SPT-selected clusters, creating mock X-ray count rates using the SZE-based masses presented for these clusters (Bleem et al. 2015; Bocquet et al. 2015). This enables a test of the photometric redshifts from our method using a sample of 29 spectroscopically confirmed SPT-selected clusters. Photometric redshifts for our cluster candidates reach a characteristic accuracy of $< \sigma_z/(1 + z) > \approx 0.010$. This performance is comparable to that of other cluster finding codes such as RedMaPPer. Moreover, the $\lambda_{\rm MCMF}$–mass distribution of SPT clusters nicely follows the behaviour of the mostly lower mass systems identified using our MCMF confirmed RASS-selected clusters.

We compare our MCMF confirmed 2RXS cluster sample to several other existing catalogues over the same portion of the sky. These include SPT, MCXC, and RedMaPPer. We could find no clear evidence of SPT clusters missing in the 2RXS sample or high-mass 2RXS clusters missing in the SPT sample. All MCXC systems were confirmed, save for one system that was flagged as a problematic cluster candidate in the original SHARC survey. A direct comparison between the RedMaPPer sample and ours enables another test. We find a single 2RXS+MCMF system that appears to be an X-ray point source associated with RS galaxies in the outskirts of a larger optical system identified by RedMaPPer. The cross-matched 2RXS+MCMF and RedMaPPer catalogue allow further tests of our photometric redshifts. The two sets of redshifts are in good agreement, exhibiting scatter similar in scale to that seen when we compare to spectroscopic redshifts. Because in this case the same raw optical data are used for both catalogues, this good agreement is a test only of the differences between the methods and therefore measures only one component of the photometric redshift error. Finally, there is a strong correlation between the RedMaPPer richnesses $\lambda_{\rm RM}$ and $\lambda_{\rm MCMF}$.

Using the best-fitting luminosity–$\lambda_{\rm MCMF}$ scaling relation, we show that the cluster sample is primarily RASS limited out to a

redshift $z \sim 0.9$ within the DES-SV data set. Given that DES-SV does not reach the full-expected DES depth, this implies that a complete RASS cluster confirmation of the DES area does not require the final DES data set. Using the average source density of RASS and our cuts for optical counterpart significance, we estimate that we will obtain a cluster sample of 1500–2500 clusters over the full DES area. The sample would be one of the largest homogeneously X-ray-selected cluster samples in the Southern hemisphere and likely remain so until the forthcoming launch of eROSITA. A cosmological analysis of our MCMF sample would be improved by a re-extraction of X-ray properties and improved calibration of the relevant mass–observable relations.

ACKNOWLEDGEMENTS

We thank Th. Boller, M. Freyberg, and H. Brunner from the MPE High Energy Group for helpful conversations. We acknowledge the support of the Max Planck Gemeinschaft Faculty Fellowship programme and the High Energy Group at MPE. Further, we acknowledge the support of the DFG Cluster of Excellence 'Origin and Structure of the Universe', the Transregio programme TR33 'The Dark Universe', the Ludwig-Maximilians-Universität and the DLR supported Euclid development project. The data processing has been carried out on the computing facilities of the Computational Center for Particle and Astrophysics (C2PAP), located at the Leibniz Supercomputer Center (LRZ).

Funding for the DES Projects has been provided by the US Department of Energy, the US National Science Foundation, the Ministry of Science and Education of Spain, the Science and Technology Facilities Council of the United Kingdom, the Higher Education Funding Council for England, the National Center for Supercomputing Applications at the University of Illinois at Urbana-Champaign, the Kavli Institute of Cosmological Physics at the University of Chicago, the Center for Cosmology and Astro-Particle Physics at the Ohio State University, the Mitchell Institute for Fundamental Physics and Astronomy at Texas A&M University, Financiadora de Estudos e Projetos, Fundação Carlos Chagas Filho de Amparo à Pesquisa do Estado do Rio de Janeiro, Conselho Nacional de Desenvolvimento Científico e Tecnológico and the Ministério da Ciência, Tecnologia e Inovação, the Deutsche Forschungsgemeinschaft and the Collaborating Institutions in the Dark Energy Survey. The Collaborating Institutions are Argonne National Laboratory, the University of California at Santa Cruz, the University of Cambridge, Centro de Investigaciones Energéticas, Medioambientales y Tecnológicas-Madrid, the University of Chicago, University College London, the DES-Brazil Consortium, the University of Edinburgh, the Eidgenössische Technische Hochschule (ETH) Zürich, Fermi National Accelerator Laboratory, the University of Illinois at Urbana-Champaign, the Institut de Ciències de l'Espai (IEEC/CSIC), the Institut de Física d'Altes Energies, Lawrence Berkeley National Laboratory, the Ludwig-Maximilians Universität München and the associated Excellence Cluster Universe, the University of Michigan, the National Optical Astronomy Observatory, the University of Nottingham, The Ohio State University, the University of Pennsylvania, the University of Portsmouth, SLAC National Accelerator Laboratory, Stanford University, the University of Sussex, Texas A&M University, and the OzDES Membership Consortium. The DES data management system is supported by the National Science Foundation under Grant Number AST-1138766. The DES participants from Spanish institutions are partially supported by MINECO under grants AYA2012-39559, ESP2013-48274, FPA2013-47986, and Centro de Excelencia Severo Ochoa SEV-2012-0234. Research leading to these results has received funding from the European Research Council under the European Union's Seventh Framework Programme (FP7/2007-2013) including ERC grant agreements 240672, 291329, and 306478.

REFERENCES

Abell G. O., 1958, ApJS, 3, 211
Bartelmann M., 1996, A&A, 313, 697
Bayliss M. B. et al., 2016, ApJS, 227, 3
Bertin E., 2006, in Gabriel C., Arviset C., Ponz D., Enrique S., eds, ASP Conf. Ser. Vol. 351, Astronomical Data Analysis Software and Systems XV. Astron. Soc. Pac., San Francisco, p. 112
Bertin E., Arnouts S., 1996, A&AS, 117, 393
Bleem L. E. et al., 2015, ApJS, 216, 27
Bocquet S. et al., 2015, ApJ, 799, 214
Boese F. G., 2000, A&AS, 141, 507
Böhringer H. et al., 2000, ApJS, 129, 435
Böhringer H. et al., 2004, A&A, 425, 367
Boller T., Freyberg M. J., Trümper J., Haberl F., Voges W., Nandra K., 2016, A&A, 588, A103
Bower R. G., Lucey J. R., Ellis R. S., 1992, MNRAS, 254, 601
Burke D. J., Collins C. A., Sharples R. M., Romer A. K., Nichol R. C., 2003, MNRAS, 341, 1093
de Haan T. et al., 2016, ApJ, 832, 95
De Propris R., Stanford S. A., Eisenhardt P. R., Dickinson M., Elston R., 1999, AJ, 118, 719
Dark Energy Survey Collaboration et al., 2016, MNRAS, 460, 1270
Desai S. et al., 2012, ApJ, 757, 83
Ebeling H., Edge A. C., Henry J. P., 2001, ApJ, 553, 668
Ebeling H. et al., 2013, MNRAS, 432, 62
Ellis R. S., Smail I., Dressler A., Couch W. J., Oemler A., Jr, Butcher H., Sharples R. M., 1997, ApJ, 483, 582
Flaugher B. et al., 2015, AJ, 150, 150
Gladders M. D., Yee H. K. C., 2000, AJ, 120, 2148
Gladders M. D., Yee H. K. C., Majumdar S., Barrientos L. F., Hoekstra H., Hall P. B., Infante L., 2007, ApJ, 655, 128
Haiman Z., Mohr J. J., Holder G. P., 2001, ApJ, 553, 545
Hennig C. et al., 2017a, MNRAS, 467, 4015
Hennig C. et al., 2017b, MNRAS, 467, 4015
Henry J. P., Mullis C. R., Voges W., Böhringer H., Briel U. G., Gioia I. M., Huchra J. P., 2006, ApJS, 162, 304
Ilbert O. et al., 2009, ApJ, 690, 1236
Kelly B. C., 2007, ApJ, 665, 1489
Laureijs R. et al., 2011, preprint (arXiv:1110.3193)
Lin Y., Mohr J. J., Gonzalez A. H., Stanford S. A., 2006, ApJ, 650, L99
Liu J. et al., 2015, MNRAS, 449, 3370
Mantz A., Allen S. W., Rapetti D., Ebeling H., 2010a, MNRAS, 406, 1759
Mantz A., Allen S. W., Ebeling H., Rapetti D., Drlica-Wagner A., 2010b, MNRAS, 406, 1773
Merloni A. et al., 2012, preprint (arXiv:1209.3114)
Moffat P. H., 1972, MNRAS, 160, 139
Navarro J. F., Frenk C. S., White S. D. M., 1997, ApJ, 490, 493
Piffaretti R., Arnaud M., Pratt G. W., Pointecouteau E., Melin J.-B., 2011, A&A, 534, A109
Predehl P. et al., 2010, in Arnaud M., Murray S. S., Takahashi T., eds, Proc. SPIE Conf. Ser. Vol. 7732, Space Telescopes and Instrumentation 2010: Ultraviolet to Gamma Ray. SPIE, Bellingham, p. 77320U
Rapetti D., Allen S. W., Mantz A., Ebeling H., 2010, MNRAS, 406, 1796
Regnault N. et al., 2009, A&A, 506, 999
Robertson A., Massey R., Eke V., 2017, MNRAS, 465, 569
Rozo E. et al., 2010, ApJ, 708, 645
Ruel J. et al., 2014, ApJ, 792, 45
Rykoff E. S. et al., 2012, ApJ, 746, 178
Rykoff E. S. et al., 2014, ApJ, 785, 104
Rykoff E. S. et al., 2016, ApJS, 224, 1

Sadat R., Blanchard A., Kneib J.-P., Mathez G., Madore B., Mazzarella J. M., 2004, A&A, 424, 1097
Saro A. et al., 2015, MNRAS, 454, 2305
Sartoris B. et al., 2014, ApJ, 783, L11
Schechter P., 1976, ApJ, 203, 297
Schlafly E. F. et al., 2012, ApJ, 756, 158
Skrutskie M. F. et al., 2006, AJ, 131, 1163
Smith R. K., Brickhouse N. S., Liedahl D. A., Raymond J. C., 2001, ApJ, 556, L91
Sommer M. W., Basu K., 2014, MNRAS, 437, 2163
Song J. et al., 2012, ApJ, 761, 22
Sunyaev R. A., Zel'dovich Y. B., 1970, Comments Astrophys. Space Phys., 2, 66
Truemper J., 1982, Adv. Space Res., 2, 241
Vikhlinin A. et al. 2009, ApJ, 692, 1060
Vikhlinin A., McNamara B. R., Forman W., Jones C., Quintana H., Hornstrup A., 1998, ApJ, 502, 558
Voges W. et al., 1999, A&A, 349, 389
Voges W. et al., 2000, VizieR Online Data Catalog, 9029, 0
Wang L., Steinhardt P. J., 1998, ApJ, 508, 483
White S. D. M., Efstathiou G., Frenk C. S., 1993, MNRAS, 262, 1023
Zacharias N., Finch C. T., Girard T. M., Henden A., Bartlett J. L., Monet D. G., Zacharias M. I., 2012, VizieR Online Data Catalog, 1322
Zenteno A. et al., 2011, ApJ, 734, 3
Zenteno A. et al., 2016, MNRAS, 462, 830

[1]*Faculty of Physics, Ludwig-Maximilians-Universität, Scheinerstr. 1, D-81679 Munich, Germany*
[2]*Max Planck Institute for Extraterrestrial Physics, Giessenbachstrasse, D-85748 Garching, Germany*
[3]*Excellence Cluster Universe, Boltzmannstr. 2, D-85748 Garching, Germany*
[4]*Department of Physics, IIT Hyderabad, Kandi, Telangana 502285, India*
[5]*Fermi National Accelerator Laboratory, P. O. Box 500, Batavia, IL 60510, USA*
[6]*CNRS, UMR 7095, Institut d'Astrophysique de Paris, F-75014, Paris, France*
[7]*Department of Physics & Astronomy, University College London, Gower Street, London WC1E 6BT, UK*
[8]*Sorbonne Universités, UPMC Univ Paris 06, UMR 7095, Institut d'Astrophysique de Paris, F-75014 Paris, France*
[9]*Laboratório Interinstitucional de e-Astronomia – LIneA, Rua Gal. José Cristino 77, Rio de Janeiro, RJ-20921-400, Brazil*
[10]*Observatório Nacional, Rua Gal. José Cristino 77, Rio de Janeiro, RJ-20921-400, Brazil*
[11]*Department of Astronomy, University of Illinois, 1002 W. Green Street, Urbana, IL 61801, USA*
[12]*National Center for Supercomputing Applications, 1205 West Clark St., Urbana, IL 61801, USA*
[13]*Kavli Institute for Particle Astrophysics & Cosmology, P.O. Box 2450, Stanford University, Stanford, CA 94305, USA*
[14]*Jet Propulsion Laboratory, California Institute of Technology, 4800 Oak Grove Dr., Pasadena, CA 91109, USA*
[15]*Department of Astronomy, University of Michigan, Ann Arbor, MI 48109, USA*
[16]*Department of Physics, University of Michigan, Ann Arbor, MI 48109, USA*
[17]*Kavli Institute for Cosmological Physics, University of Chicago, Chicago, IL 60637, USA*
[18]*SLAC National Accelerator Laboratory, Menlo Park, CA 94025, USA*
[19]*Center for Cosmology and Astro-Particle Physics, The Ohio State University, Columbus, OH 43210, USA*
[20]*Department of Physics, The Ohio State University, Columbus, OH 43210, USA*
[21]*Astronomy Department, University of Washington, Box 351580, Seattle, WA 98195, USA*
[22]*Cerro Tololo Inter-American Observatory, National Optical Astronomy Observatory, Casilla 603, La Serena, Chile*
[23]*Australian Astronomical Observatory, North Ryde, NSW 2113, Australia*
[24]*Departamento de Física Matemática, Instituto de Física, Universidade de São Paulo, CP 66318, CEP 05314-970, São Paulo, SP, Brazil*
[25]*Department of Physics and Astronomy, University of Pennsylvania, Philadelphia, PA 19104, USA*
[26]*Department of Astrophysical Sciences, Princeton University, Peyton Hall, Princeton, NJ 08544, USA*
[27]*Institució Catalana de Recerca i Estudis Avançats, E-08010 Barcelona, Spain*
[28]*Institut de Física d'Altes Energies (IFAE), The Barcelona Institute of Science and Technology, Campus UAB, E-08193 Bellaterra (Barcelona), Spain*
[29]*Department of Physics and Astronomy, Pevensey Building, University of Sussex, Brighton BN1 9QH, UK*
[30]*Centro de Investigaciones Energéticas, Medioambientales y Tecnológicas (CIEMAT), Madrid, Spain*
[31]*Instituto de Física, UFRGS, Caixa Postal 15051, Porto Alegre, RS-91501-970, Brazil*
[32]*School of Physics and Astronomy, University of Southampton, Southampton SO17 1BJ, UK*
[33]*Universidade Federal do ABC, Centro de Ciências Naturais e Humanas, Av. dos Estados, 5001, Santo André, SP 09210-580, Brazil*
[34]*Computer Science and Mathematics Division, Oak Ridge National Laboratory, Oak Ridge, TN 37831, USA*

This paper has been typeset from a TEX/LATEX file prepared by the author.